

21 Other physics beyond the Standard Model

21.1 Introduction

This chapter discusses signals for a variety of possible physics in extensions of the Standard Model. Technicolor models replace the elementary Higgs bosons of the Standard Model or SUSY with dynamical condensates. The simplest such models predict flavour changing neutral currents and other violations of precision electroweak data. Nevertheless, the basic idea of technicolor remains viable, although there is no 'standard' technicolor model. Technicolor solves the hierarchy problem if the mass scale is less than about 1 TeV, so it should be observable at the LHC. Excited quarks, leptoquarks, and contact interactions are not predictions of any specific model but are examples of possible new physics. New gauge bosons are typically predicted by any extension of the electroweak gauge group. Finally, monopoles might explain the quantisation of charge. The new energy regime opened up at the LHC makes it interesting to search for these and other types of new physics.

21.2 Search for technicolor signals

Technicolor theory (TC) provides a dynamical means of breaking electroweak symmetry [21-1]. It assumes the existence of technifermions possessing a technicolor charge and interacting strongly at a high scale. Chiral symmetry is broken by techniquark condensates giving rise to Goldstone bosons, the technipions, which are the longitudinal degrees of freedom of the W and Z gauge bosons. The theory has been extended (extended technicolor, or ETC) to allow the generation of mass for the known fermions [21-2]. In order to account for the absence of FCNC's, the coupling constant is required to 'walk', rather than 'run'. To achieve a walking α_{TC} multi-scale technicolor models contain several representations of the fundamental family, and lead to the existence of technihadron resonances accessible at LHC energies. Such models [21-3], and others [21-4] are constrained by precision electroweak data [21-5], but are not necessarily excluded [21-6][21-7]. However, the constraints from these measurements make it unnatural to have a large top quark mass. In top-colour-assisted technicolor (TC2) models [21-8][21-9], the top quark mass arises in large part from a new strong top-colour interaction, which is a separate broken gauge sector.

The search for technipions and associated ETC gauge bosons is discussed in recent references [21-3][21-10]. In this section, the possible observation of these resonances by using the ATLAS detector is investigated. In particular, the search for a ($I=1, J=1$) techni-rho resonance decaying to a pair of gauge bosons, or to a techni-pion and a gauge boson is presented. Single production of a technipion may be detected under particular conditions, if it decays to heavy quarks. A clean signal of another vector resonance can also be obtained from the process $pp \rightarrow \omega_T \rightarrow \pi_T^0 \gamma$. Finally, the usefulness of forward jet tagging is discussed for studies of such resonances, when produced by gauge boson pair fusion. Although certain models, with a given set of parameters, are used as reference, the signals studied here can be considered generic in any model which predicts resonances. Therefore, results are presented in each case not only relative to the reference model, but also as lower limits on the $\sigma \times \text{BR}$ required for observation of the resonance at the five standard deviation level.

The signals and backgrounds discussed in this note have been generated with PYTHIA 6.1 [21-11]. The trigger acceptance as well as the detector acceptance and resolution effects were simulated with the parametrised Monte Carlo program ATLFast 1.53 [21-12], with default values of the parameters. In particular, jets were reconstructed with the cone algorithm, requiring a cone radius of 0.4 and a minimum E_T of 15 GeV. Low luminosity conditions ($L = 10^{33} \text{ cm}^{-2} \text{ s}^{-1}$) were assumed for the energy resolution of jets. Leptons were required to be isolated, meaning that their electromagnetic clusters in the calorimeter were separated from other clusters by $\Delta R > 0.4$ and $E_T < 10$ GeV in a cone $\Delta R = 0.2$ around the lepton. Jets were identified as b -jets if a b -quark of $p_T > 5$ GeV was within a cone radius of 0.2 of the direction of the jet. For b -tagging efficiencies and rejection factors, 53% global efficiency and 91% global rejection of non- b jets are assumed.

21.2.1 Technicolor signals from $q\bar{q}$ fusion

The model adopted here is that of multiscale technicolor [21-13][21-14], with the technicolor group $SU(N_{TC})$, $N_{TC} = 4$ and two isotriplets of technipions. The mixing angle between the longitudinal gauge bosons and the technipions, $|\Pi_T\rangle = \sin \chi |W_L\rangle + \cos \chi |\pi_T\rangle$, has the value $\sin(\chi) = 1/3$, the decay constant of the mixed state $F_T = F_\pi \sin(\chi) = 82$ GeV, and the charge of the up-type (down-type) technifermion $Q_U = 1$, ($Q_D = 0$). This model is incorporated in PYTHIA6.1 [21-11]. It should be noted that the decay widths of the ρ_T and the ω_T depend upon $(Q_U + Q_D)$ and upon the masses assumed. The branching ratios assumed in the present analysis do not account for possible decays to transversely polarised gauge bosons, recently calculated in [21-15].

The decay channels of a techni-rho (ρ_T) depend on the assumed masses of the techniparticles. Different ‘typical’ mass scenarios have been considered here. One case, $m_\rho = 220$ GeV and $m_\pi = 110$ GeV was chosen because it has been studied for the Tevatron [21-3][21-13]. Other cases are representative of what one may expect to probe at the LHC. It is also assumed in the present analysis that the π_T coupling (and therefore its decay) to the top quark is very small, as may be expected in TC2 theories. This is only an approximation. A more general case will be considered in the analysis of a $t\bar{t}$ resonance.

21.2.1.1 $\rho_T^\pm \rightarrow W^\pm Z \rightarrow l^\pm \nu l' \bar{l}'$

This decay could be the cleanest channel for detection of a technirho. The resonant production of WZ decaying to two leptons and two jets has been considered in the framework of the chiral Lagrangian model in Chapter 19.4.2. Table 21-1 shows the parameters assumed here for the techniparticles and the $\sigma \times \text{BR}$ in the multiscale model. The cross sections account for a preselection on the mass of the hard scattering subsystem ($\hat{m} > 150, 300, 600$ GeV for $m_{\rho_T} = 220, 500$ and 800 GeV respectively.)

The only background which needs to be considered is the continuum production of WZ gauge bosons, with a cross section of 21 pb. The following cuts are applied:

- The lepton trigger serves as a preselection. At least three charged leptons are required here, ($E_T > 20$ GeV for electrons and $p_T > 6$ GeV for muons), two of which must have the same flavour and opposite charge¹.

1. The lepton detection efficiency was assumed to be 100%, the results in this section are slightly optimistic as an efficiency of 90% is expected.

Table 21-1 Masses and parameters for technicolor cases considered.

Case	$m\rho_T$ (GeV)	$m\pi_T$ (GeV)	$\Gamma\rho_T$ (GeV)	BR ($\rho_T \rightarrow WZ$)	$\sigma(\text{production})$, pb
(a)	220	110	0.93	0.13	80
(e)		110	67	0.014	7.1
(b)	500	300	4.5	0.21	4.4
(f)		500	1.1	0.87	4.4
(g)		110	130	0.013	0.82
(d)		250	77	0.022	0.74
(h)	800	300	52	0.032	0.80
(c)		500	7.6	0.22	0.77

- The invariant mass of the lepton pair with the same flavour and opposite sign should be close to the that of the Z: $m_{l+l-} = m_Z \pm 5$ GeV.
- The longitudinal momentum of the neutrino is calculated, within a two fold ambiguity, from the missing transverse energy and the momentum of the unpaired lepton assuming an invariant mass $m_{l\nu} = m_W$. Both solutions are given a weight of 0.5. Once the W and Z are reconstructed, their transverse momentum is required to be larger than 40 GeV.
- Only events for which the decay angle with respect to the direction of the WZ system (ρ_T) in its rest frame is $|\cos \hat{\theta}| < 0.8$ are accepted. This variable is sensitive to the polarisation of the ρ_T (see Figure 21-1).

Table 21-2 shows the significance for all the cases considered. The number of signal and background events is counted in mass regions around the ρ_T peak. The selected regions were [210-240], [460-560] and [740-870] GeV for $m_{\rho_T} = 220, 500$ and 800 GeV respectively. No evident signal is observed for cases (e), (g) and (h) (see Figure 21-2), principally because the ρ_T resonance is wide. Table 21-2 shows also the lower limit on $(\sigma \times BR)$ required for a 5σ significance, from which one could infer the potential of observability for a different assumed branching ratio. Since this signal is based only on lepton reconstruction, the significance can be expected to scale approximately as the square root of the integrated luminosity, even in the presence of pile-up.

Table 21-2 Expected significance for the signal $\rho_T^\pm \rightarrow W^\pm Z \rightarrow l^\pm \nu l' t$, with 30 fb^{-1} . The mass bins used are given in the text.

case	(a)	(e)	(b)	(f)	(g)	(h)	(c)
S/\sqrt{B}	41.8	0.8	18	77	0.28	0.98	8.2
$\sigma \times BR$ (fb), model	160	1.04	13	54	0.15	0.36	0.25
$\sigma \times BR$ (fb), for 5σ significance	19	6.5	3.6	3.5	2.6	1.8	1.5

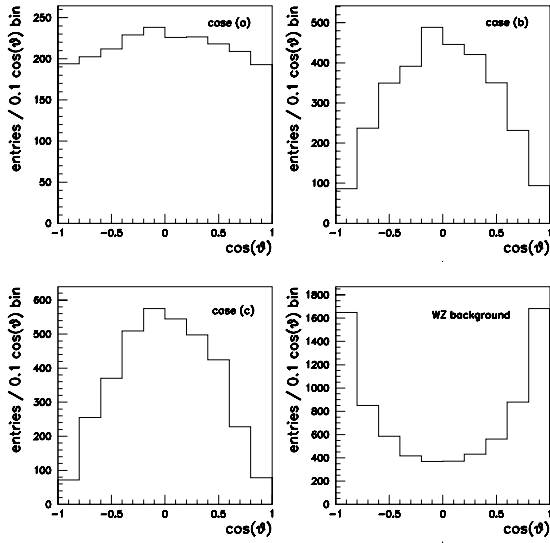


Figure 21-1 $\rho_T^\pm \rightarrow W^\pm Z \rightarrow l^\pm \nu l' T$: Distribution of decay angles of the ρ_T candidates for three cases of ρ_T production and for WZ background.

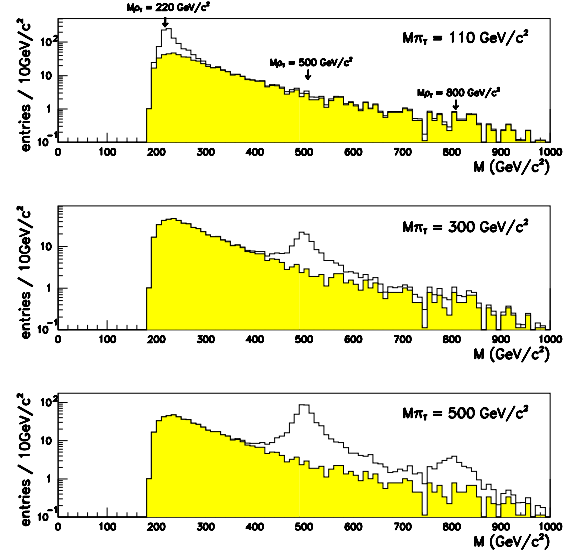


Figure 21-2 $\rho_T^\pm \rightarrow W^\pm Z \rightarrow l^\pm \nu l' T$: Reconstructed $W^\pm Z^0$ invariant mass. The solid line is for the ρ_T signal and the filled area for the WZ background. The three diagrams show the different ρ_T for the cases (a) (e) (g), (b) (h), and (f) (c).

21.2.1.2 $\rho_T^\pm \rightarrow \pi_T^\pm Z \rightarrow b q l^+ l^-$

Here, the technipion decays to b and c quarks (a c -quark jet will not be distinguished from a light quark jet in this analysis). Only cases (b), (c) and (d), defined in Table 21-1 are considered here. Given the parameters chosen for the model, the branching ratios $BR(\rho_T^\pm \rightarrow \pi_T^\pm Z^0)$ are 39.8%, 38.2% and 13.0% respectively. In all cases, π_T^\pm decays to $c\bar{b}$ (or $b\bar{c}$) 92% of the time (assuming that the coupling to the top quark is negligible).

The principal backgrounds are: Z + jets (with $p_T > 100$ GeV, consisting of $qq \rightarrow gZ$, $qg \rightarrow qZ$ and $qq \rightarrow ZZ$), $t\bar{t}$ (with $p_T > 80$ GeV), and continuum WZ production (with $p_T > 30$ GeV). The cuts used in this analysis are the following:

- Two same flavour, opposite charge leptons required, with $p_T(l_1) > 60$ GeV and $p_T(l_2), 20$ GeV. The invariant mass of the lepton pair should be close to the mass of the Z , i.e. $|m_{ll} - m_Z| < 5$ GeV.
- One identified b -jet is required. The highest p_T b -jet is assumed to come from the technipion decay. It must satisfy the conditions: $|\eta_b| < 2$ and $p_T^b > 100$ GeV.
- At least one jet, not identified as a b -jet, is required. The highest energy jet is the candidate. It must satisfy $|\eta_j| < 2$ and $p_T^j > 100$ GeV.
- The low mass regions are excluded: $m_{bj} > 150$ GeV and $m_{llbj} > 300$ GeV. In the rest frame of the $llbj$ system (the ρ_T), only events for which the angle of decay with respect to the direction of the ρ_T is $|\cos \hat{\theta}_{bj}| < 0.6$ are accepted. This angle is sensitive to the polarisation of the ρ_T .

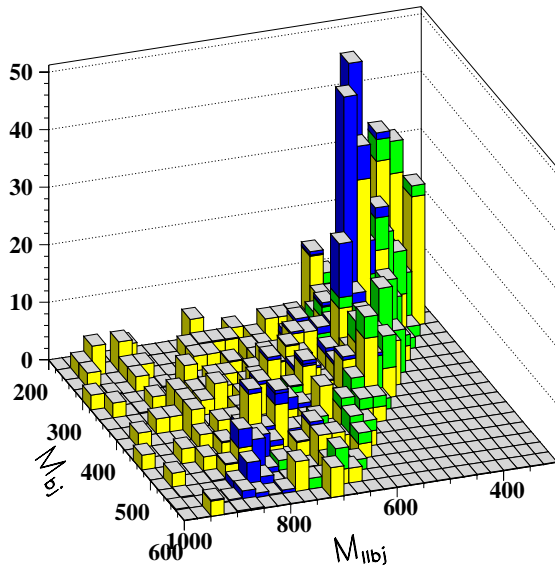


Figure 21-3 Reconstructed masses of ρ_T candidates and π_T candidates in the decay $\rho_T^\pm \rightarrow \pi_T^\pm Z \rightarrow b q l^+ l^-$. The Z+jets background is in light shade, and the $t\bar{t}$ background in darker shade. The two cases (b) and (c) are shown in dark. Statistical fluctuations are over-estimated.

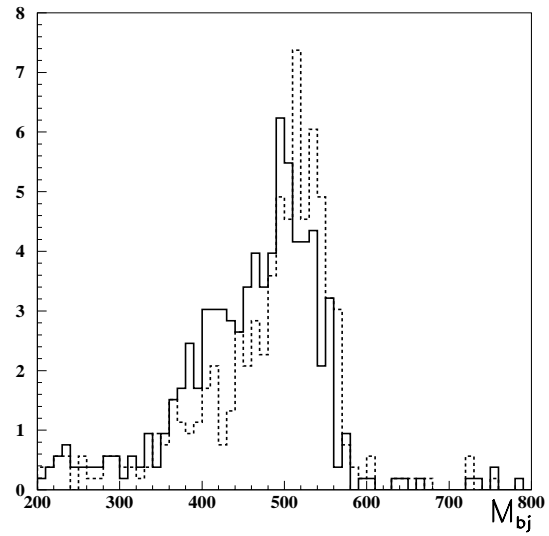


Figure 21-4 $\rho_T \rightarrow \pi_T Z \rightarrow b q l^+ l^-$: Comparison of reconstructed M_{bj} for jet cones of size $\Delta R = 0.4$ (full histogram) and $\Delta R = 0.7$ (dashed histogram). Case b is shown.

Figure 21-3 shows the signals and backgrounds expected with the above selection after three years of low luminosity running (integrated luminosity of 30 fb^{-1}). Because of the large weight of the backgrounds, statistical fluctuations are exaggerated in the figure. Cases (b) and (c) give clear signals above background, but case (d) is not resolved from background not only because of its small number of events, but also because of the larger width, 77 GeV, of the resonance.

A better mass resolution of the two jet system would considerably improve the signal to background ratio. The difference in the reconstructed masses m_{ρ_T} and m_{π_T} is better resolved than the individual masses separately, since uncertainties in jet pair mass measurement largely cancel. An improved jet pair resolution can be achieved by choosing a larger cone for jet reconstruction. Figure 21-4 shows the effect of selecting a value of $\Delta R = 0.7$ instead of $\Delta R = 0.4$. However, by doing so, one would become more susceptible to pile-up from minimum bias events, and other detector effects. In order to extract the significance of the signals (Table 21-3), the number of signal and background events are counted in mass regions around the signal peak in the following way: for cases (b), (c) and (d), the selected regions were $[m_{\rho_T} - m_{\pi_T}, m_{\pi_T}] = [175-230, 200-350]$, $[250-350, 350-600]$ and $[420-620, 190-280]$ respectively (in GeV). It was verified that the results do not change significantly if a cone of size $\Delta R = 0.7$ is used. The systematic error due to the uncertainty in the shape of the background is not included.

Table 21-3 $\rho_T \rightarrow \pi_T Z^0 \rightarrow b\bar{q}l\bar{l}$: Number of signal / Z +jets / $t\bar{t}$ events around the mass peak (see text) of the signal after the application of cuts. The last two lines give the $\sigma \times BR$ predicted by the model with the assumed values of the parameters, as well as the $\sigma \times BR$ required for a 5σ significance, with 30 fb^{-1} .

	case (b): $m(\rho_T)=500, m(\pi_T)=300 \text{ GeV}$	case (c): $m(\rho_T)=800, m(\pi_T)=500 \text{ GeV}$	case (d): $m(\rho_T)=800, m(\pi_T)=250 \text{ GeV}$
Number of events	115/148/17	48/43/2	11.5/49/0
S/\sqrt{B}	8.9	7.1	1.6
$\sigma \times BR$ model	0.104	0.018	0.0059
$\sigma \times BR$ for 5σ	0.058	0.013	0.018

21.2.1.3 $\rho_T^\pm \rightarrow W^\pm \pi_T^0 \rightarrow l \nu b \bar{b}$

With the multiscale technicolor model parameters used, the branching ratio $BR(\rho_T^\pm \rightarrow W^\pm \pi_T^0) = 36.3\%$, 38.2% and 13.2% for cases (b), (c) and (d) respectively. The π_T^0 decays 90% of the time to $b\bar{b}$ (assuming that the $t\bar{t}$ channel is closed, as in the TC2 model). It is to be noted, however, that decay of a coloured neutral technipion to a pair of gluons may have a dominant branching ratio. This case has been analysed for Tevatron energy [21-16]. The backgrounds considered here are: $t\bar{t}$, $W + jets$ (consisting of: $qq \rightarrow W$, $qq \rightarrow gW$, $qq \rightarrow WW$ and $qg \rightarrow qW$), Z +jets and WZ .

In the present analysis events are selected according to the following criteria:

- A preselection: one lepton having $p_T > 30 \text{ GeV}$ and two reconstructed b jets are required in the central region, $|\eta| < 2$. The most energetic b -jet must have $p_T > 100 \text{ GeV}$ and the other $p_T > 50 \text{ GeV}$. The missing transverse energy should be $E_T^{\text{miss}} > 50 \text{ GeV}$.
- Efficient reduction of the dominant $t\bar{t}$ background can be achieved by applying a jet veto. No extra jet, with $p_T > 40 \text{ GeV}$, besides the two b -jets is allowed.
- The W is reconstructed from the lepton and E_T^{miss} four-momenta (the longitudinal momentum of the neutrino is calculated to give the correct W mass, up to a two-fold ambiguity). The two corresponding solutions for the reconstructed mass of the ρ_T must not differ significantly: $|m_{l\nu b\bar{b}}(1) - m_{l\nu b\bar{b}}(2)| < 80 \text{ GeV}$. This cut is found to be efficient at rejecting events which do not contain a W and for which the two solutions are very different. Only events having $m_{b\bar{b}} > 150 \text{ GeV}$ and $m_{l\nu b\bar{b}} > 300 \text{ GeV}$ are kept.
- For each of these solutions, the following cut is applied: in the rest frame of the $l\nu b\bar{b}$ system, the decay angle with respect to the direction of the ρ_T must be $|\cos\hat{\theta}_{l\nu b\bar{b}}| < 0.6$. The importance of this cut is seen in Figure 21-5.

Figure 21-6 shows the signals and backgrounds expected with the above selection after 30 fb^{-1} of integrated luminosity. Both solutions are included in the histogram, with weight 0.5 each. Clear signals can be seen above background for some of the above cases, although poor $m_{b\bar{b}}$ resolution is obtained. These could be used to confirm discovery in the channel discussed above. The significance obtained for the signals is given in Table 21-4. Also shown in the table are the $\sigma \times BR$ required for a 5σ significance. The uncertainty in the shape of the background can be an important systematic error.

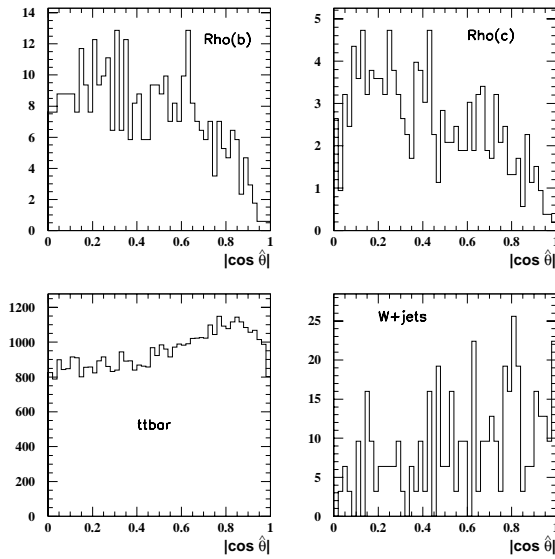


Figure 21-5 $\rho_{\tau^\pm} \rightarrow W^\pm \pi_{\tau^0} \rightarrow l^+ \nu b \bar{b}$: Distribution of $|\cos \hat{\theta}_{l\nu b\bar{b}}|$ for cases (b) and (c) as well for the $t\bar{t}$ and W +jets backgrounds.

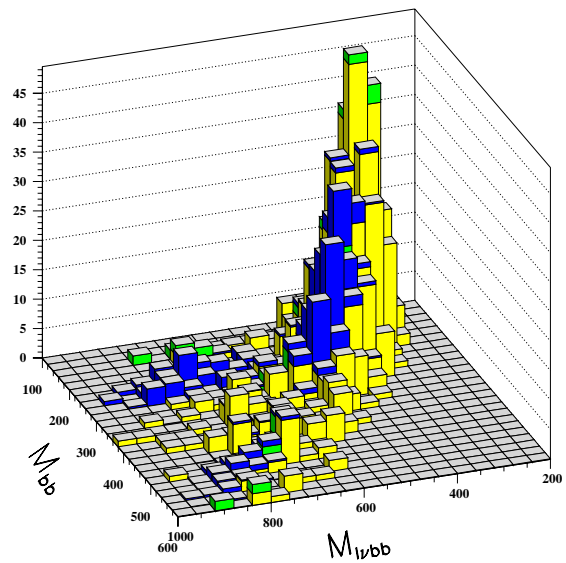


Figure 21-6 Reconstructed mass of the ρ_{τ} candidates vs mass of the ρ_{τ} candidates for the channel $\rho_{\tau} \rightarrow W^\pm \pi_{\tau^0} \rightarrow l^+ \nu b \bar{b}$. From lightest to darkest: W + jets background, $t\bar{t}$ background and the signals for three cases (b), (c) and (d). The statistical fluctuations are exaggerated.

Table 21-4 $\rho_{\tau^\pm} \rightarrow W^\pm \pi_{\tau^0} \rightarrow l^+ \nu b \bar{b}$: Number of signal/ $t\bar{t}$ / (W +jets and Z +jets) events around the mass peak (see text), after the application of cuts. The last two lines give the $\sigma \times BR$ predicted by the model, with the assumed values of the parameters, as well as the $\sigma \times BR$ required for a 5σ significance of the signal, for an integrated luminosity of 30 fb^{-1}

	case (b) $m(\rho_{\tau})=500, m(\pi_{\tau})=300 \text{ GeV}$	case (c) $m(\rho_{\tau})=800, m(\pi_{\tau})=500 \text{ GeV}$	case (d) $m(\rho_{\tau})=800, m(\pi_{\tau})=250 \text{ GeV}$
Number of events	86/165/5	24/118/10	12/5/0
S/\sqrt{B}	6.6	2.1	5.3
$\sigma \times BR$ (pb), model	0.336	0.064	0.021
$\sigma \times BR$ (pb), 5σ	0.255	0.15	0.02

21.2.1.4 $b \bar{b}$ resonance

Single production of pseudo-Goldstone bosons such as η_8 is observable, given a large enough cross section. Coloured technipions are, in particular, more likely to be detected since colour counting factors make their production cross section through gg fusion larger than for colour singlet ones. The decay to gg pairs compete, however, with the $b\bar{b}$ channel and may actually

dominate. Other $b\bar{b}$ resonances are predicted by topcolor models, where the topgluon splits into heavy quarks. The mass reach of such topgluons at the Tevatron (2 fb^{-1}) has been estimated at close to 1 TeV, depending on the width [21-17].

η_8 production is implemented in PYTHIA according to the one-family model [21-18][21-19]. The production mechanism is similar to a Standard Model Higgs boson via gg fusion, but is enhanced by the large number of techniquarks that can appear in the loop. This process is used here to estimate the observability of a generic $b\bar{b}$ resonance. The mass has been chosen to be 300 GeV, *i.e.* below the $t\bar{t}$ threshold. Generic vector resonances, such as a topgluon, of masses 500, 1000 and 2000 TeV are also studied. The backgrounds considered for this process are: hard QCD and $t\bar{t}$.

To extract the signal, the only selection was to require at least two identified b -jets with a minimum value of p_T in the region $|\eta| < 2$. For a 300 GeV resonance, LVL1 trigger J75 x 3 will be required (see Chapter 11.3.2), whereas for a 500 GeV resonance or above, single jet trigger J180 will suffice. (A prescaled single jet trigger could also be used.) Events having a third high p_T jet are rejected; the threshold is shown in Table 21-5 which also shows the required $\sigma \times \text{BR}$ for a 5σ discovery limit. In this study, the assumed intrinsic widths of the resonances were very narrow. For a wider resonance, the intrinsic width must be added in quadrature with σ_m , shown in Table 21-5 and a new estimate of $\sigma \times \text{BR}$ can be obtained. In each case, the resonance would be seen as a small, but statistically significant peak, on top of a large, steeply falling, background.

Table 21-5 Discovery limits, after 30 pb^{-1} , for narrow $b\bar{b}$ resonances of different masses, after cuts on the minimum p_T of the reconstructed b jets, and a maximum p_T of any third jet. Also shown is the approximate width of the reconstructed resonance.

$m_{b\bar{b}}$	$p_{T\text{min}}(b_1/b_2)$	$p_{T3}(\text{max})$	$\sigma_m(\text{GeV})$	$\sigma \times \text{BR}(5\sigma)(\text{pb})$
300	75/75	100	37	13
500	180/50	50	60	7.0
1000	200/100	100	70	0.57
2000	300/200	100	160	0.11

21.2.1.5 $t\bar{t}$ resonances

The general case of $t\bar{t}$ resonances is discussed in Section 18.1.4.2. Here, the case of single production of a technipion, sufficiently massive to decay to $t\bar{t}$ pairs, $m_{t\bar{t}} = 500 \text{ GeV}$, is studied. Although the decay of a technipion to $t\bar{t}$ is highly suppressed in topcolor assisted technicolor models, other resonances, such as a topgluon are predicted in this model. As in Section 21.2.1.4 above, the process of η_8 production as implemented in PYTHIA is used here. An intrinsic width $\Gamma (= 2.35 \sigma_m)$ of 57 GeV is assumed for this generic resonance.

The backgrounds considered are (i) W +jets (generated with $\hat{p}_T > 80 \text{ GeV}$) – Only events having at least one lepton and one b -jet (before b -tagging) have been generated for this analysis (ii) $t\bar{t}$, with a requirement of $\hat{p}_T > 80 \text{ GeV}$ – Only events with one lepton have been generated; and (iii) hard QCD (with $\hat{p}_T > 80 \text{ GeV}$ and $\hat{s} > (200 \text{ GeV})^2$). The cuts applied at generator level do not affect significantly the results below.

The mass of the resonance is reconstructed by looking for the channel $t\bar{t} \rightarrow l\nu b\bar{b}jj$. The following selection criteria are applied:

- One lepton is required for the trigger, with $p_T > 20$ GeV, within $|\eta| < 2$.
- Two b jets are required, with $p_T > 60$ GeV and 40 GeV respectively, and within $|\eta| < 2$. Two additional jets, not identified as b -jets are required, with $p_T > 50$ and 40 GeV, also within $|\eta| < 2$.
- E_T^{miss} must be greater than 20 GeV.

At that point, the W from the $t \rightarrow Wb \rightarrow l\nu b$ decay is reconstructed, using E_T^{miss} and the lepton momentum. There is a two-fold ambiguity in the solution. There is also a two-fold ambiguity in assigning the two highest p_T b -jets to the two highest energy light-quark jets. These ambiguities are resolved by choosing the solution that gives top masses closest to the true mass of the top (175 GeV). The cut is then $160 < m_t^l < 195$ GeV and $160 < m_t^h < 220$ GeV, where m_t^l and m_t^h are the reconstructed masses of the top quarks for which the W decays leptonically and hadronically, respectively.

This simple procedure gives top-mass resolution as shown in Figure 21-7. The $t\bar{t}$ resonance mass is then reconstructed $t\bar{t}$ with a resolution of about 57 GeV. The required $\sigma \times \text{BR}$ for a 5σ discovery limit is then 9.9 pb, for an integrated luminosity of 30 fb^{-1} .

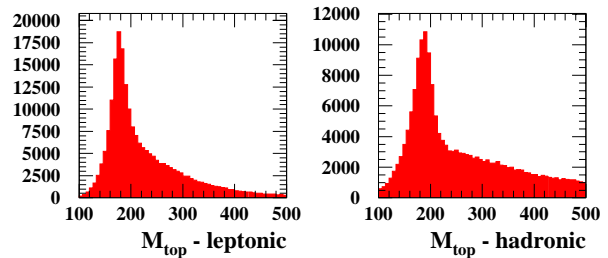


Figure 21-7 $t\bar{t}$ resonance: reconstructed masses of top in $t\bar{t}$ decays. The left histogram shows the mass of the top for which the W decays leptonically and the one on the right shows the mass of the other top, with leptonic decay of the W .

Table 21-6 shows the result of extending this study to larger masses. It shows the rates needed for these heavier cases to be found by ATLAS.

Table 21-6 Masses and natural widths assumed for the study of technicolor η_8 resonances. Also shown are the minimum values of $\sigma \times \text{BR}$ necessary for a 5σ discovery significance of $\eta_8 \rightarrow t\bar{t}$ for integrated luminosities of 10 fb^{-1} and 100 fb^{-1} .

$m(t\bar{t})$ [GeV]	$\Gamma(t\bar{t})$ [GeV]	$\sigma \times \text{BR}$ [pb]	
		10 fb^{-1}	100 fb^{-1}
500	57	17.0	5.5
750	107	12.0	3.8
1000	152	5.0	1.6

21.2.1.6 $\omega_T \rightarrow \gamma \pi_T^0 \rightarrow \gamma b \bar{b}$

The ω_T^0 particle is a vector particle of isospin 0. One of its clean decay modes is $\omega_T \rightarrow \gamma \pi_T^0$. A search for this particle has been performed by CDF [21-20]. Here, two cases have been investigated: (i) $m_{\omega_T} = 500$ GeV, with width 0.32 GeV and $m_{\pi_T} = 300$ GeV. The cross section for production is 0.51 pb, according to the model used here [21-13][21-14], as implemented in PYTHIA, and the branching ratio to $\gamma \pi_T^0$ is 87%.;(ii) $m_{\omega_T} = 800$ GeV with width 1.0 GeV and $m_{\pi_T} = 500$ GeV. The cross section for production is 0.093 pb, and the branching ratio to $\gamma \pi_T^0$ is 94%. This assumed branching ratio does not account for decays to transversely polarised gauge bosons [21-15].

For the simulation of the background, a Monte Carlo program for $\gamma b \bar{b}$, provided by [21-21] was used. Also included are backgrounds from $qq \rightarrow \gamma g$, $qg \rightarrow \gamma q$ and $g g \rightarrow \gamma g$. Backgrounds from misidentified photon jets are not taken into account. The rejection that ATLAS obtains is large enough so that these backgrounds due to misidentification are small. (See the discussion of $h \rightarrow \gamma \gamma$ in Chapter 19.2.2)

To extract the signal, the selection criteria are:

- the presence of one photon with $p_T^\gamma > 50$ GeV within $|\eta| < 2$;
- the presence of two identified b -jets, each having $p_T > 40$ GeV and falling within $|\eta| < 2$;
- the difference in azimuthal angles between the two b -jets must be > 2 radians, as they are expected to be mostly back to back for a heavy decaying system.

With these selection criteria, the signals that remain are shown in Figure 21-8. There is a significant signal for both masses of ω_T . Table 21-7 gives the observed significances and $\sigma \times \text{BR}$ required for a 5σ significance after 30 fb^{-1} for both the lower and higher mass ω_T in the mass windows $[250 < m_{bb} < 350; 180 < m_{\gamma bb} < 220]$ and $[400 < m_{bb} < 600; 280 < m_{\gamma bb} < 230]$ respectively.

21.2.2 Signals from vector boson fusion

Production of the ρ_T by vector boson fusion is potentially very interesting since it probes the coupling to gauge bosons and since the requirement of forward jets resulting from the scattered primary quarks provides a powerful method of background rejection.

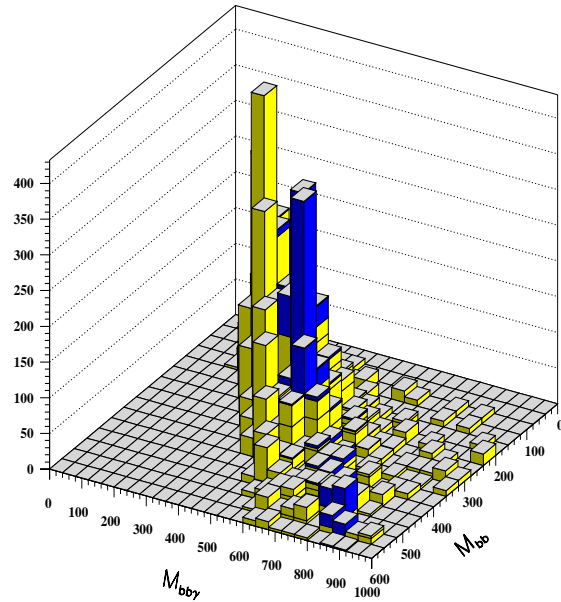


Figure 21-8 $\omega_T \rightarrow \gamma \pi_T^0 \rightarrow \gamma b \bar{b}$: Reconstructed masses of $b\bar{b}$ -jet system versus the mass of the $\gamma b\bar{b}$ system. Two scenarios are considered for the signal: ω_T of masses 800 GeV and 500 GeV decaying to π_T of masses 500 GeV and 300 GeV respectively. The signals are in dark shade. In light shade is the prompt photon background.

Table 21-7 $\omega_T \rightarrow \gamma \pi_T^0 \rightarrow \gamma b \bar{b}$: Number of signal/ γ +jets events around the mass peak of the signal, for an integrated luminosity of 30 fb^{-1} . The $\sigma \times BR$ predicted by the model, with the assumed values of the parameters, and the $\sigma \times BR$ required for a 5σ significance of the signal are also shown.

	$m(\omega_T)=500 \text{ GeV}$	$m(\omega_T)=800 \text{ GeV}$
Number of events	612/105	174/24
S/\sqrt{B}	60	35
$\sigma \times BR$ (pb), model	0.161	0.033
$\sigma \times BR$ (pb) 5σ	0.013	0.0046

As an example of this calculation, the same case as Section 21.2.1.3: $\rho_T^\pm \rightarrow W^\pm \pi_T^0 \rightarrow l \nu b \bar{b}$, ($l = \mu, e$) with $m_{\rho_T} = 800 \text{ GeV}$ and $m_{\pi_T} = 500 \text{ GeV}$ (case (c)) is considered here. For this process, $\sigma \times BR$ is about 2.5 fb [21-22]. Because it involves the $W Z \rho_T$ vertex, as well as the $\rho_T W \pi_T$ vertex, the cross section depends sensitively on the assumed value of the mixing angle χ between the longitudinal gauge boson and the technipion. The same background Monte Carlo samples as in Section 21.2.1.3 are used. The following cuts are applied on both the signal and background.

- The presence of at least one lepton ($p_T > 20 \text{ GeV}$) and two reconstructed b -jets ($p_T > 50 \text{ GeV}$) is required in the central region $|\eta| < 2$. The missing transverse energy must be greater than 20 GeV .
- Since the ρ_T is colour neutral, a central jet-veto ($|\eta| < 2$) helps reject the $t\bar{t}$ background.
- A forward and a backward jet are required, with $p_T > 80 \text{ GeV}$ and $1.5 < |\eta| < 3.5$ for the first jet and $p_T > 50 \text{ GeV}$ and $1 < |\eta| < 4$ for the second jet.

Given a $\sigma \times BR$ of only 2.5 fb , the resulting signal would be 2.6 events on a background of about 5.6, for an integrated luminosity of 30 fb^{-1} . This process of vector boson fusion with forward tagging of jets could complement the $q\bar{q}$ fusion process, but would not be a discovery channel unless the $\sigma \times BR$ is at least 10 fb .

21.2.3 Conclusion

The ATLAS detector will be sensitive to the new resonances predicted in technicolor theory, up to the TeV range. Although the parameter space is very large, the number of potential channels allows for combinations of signatures to help in understanding the nature of the resonances, and determine the possible existence of techniparticles.

21.3 Search for excited quarks

The replication of three generations of quarks and leptons suggests the possibility that they are composite structures made up of more fundamental constituents. The existence of such quark and lepton substructure leads one to expect a rich spectrum of new particles with unusual quantum numbers such as excited quarks and leptons, leptoquarks, diquarks, dileptons, *etc.* Since no satisfactory, theoretically consistent composite model yet exists, here the excited quarks are taken into account as composite particles. The regions of compositeness scale Λ are given as

- $\Lambda \gg \sqrt{\hat{s}}$, contact and anomalous interactions;
- $\Lambda \ll \sqrt{\hat{s}}$, resonance productions, excited quarks or di-quarks, pair or single production of new particles;
- $\Lambda \approx \sqrt{\hat{s}}$, model dependent interactions.

In this study, it is assumed that the compositeness scale Λ is less than the LHC energy. Gauge interactions are assumed to dominate over contact interactions when the masses of excited quarks are equal to the compositeness scale. Only, spin-1/2 excited states of the first generation, $q^* = u^*, d^*$ are considered. The coupling between excited (right-handed) quarks, ordinary (left-handed) quarks and gauge bosons is given by the effective Lagrangian of the magnetic moment type [21-23];

$$L = \frac{1}{2\Lambda} \bar{q}^* \sigma^{\mu\nu} \left(g_s f_s \frac{\lambda}{2} G_{\mu\nu}^a + g f \frac{\tau}{2} \cdot W_{\mu\nu} + g' f' \frac{Y}{2} B_{\mu\nu} \right) q_L$$

where $G_{\mu\nu}^a$, $W_{\mu\nu}$ and $B_{\mu\nu}$ are the field-strength tensors of the SU(3), SU(2) and U(1) gauge fields; λ_a , τ and Y are the corresponding gauge structure constants; and g_s , g and g' are the gauge coupling constants. Finally, f_s , f and f' are parameters determined by the composite dynamics.

The production of the first generation excited quarks u^*, d^* by quark-gluon fusion process $qg \rightarrow q^*$ is studied at the LHC [21-24]. Here, the quark from q^* decay was assumed to correspond to the leading jet with the highest transverse momenta in the event. The signal consists of a high energy jet resulting from the hadronisation of the final state quark and a photon which form a peak in photon+jet invariant mass distribution $m_{\gamma j}$.

CDF excludes the following mass ranges for the excited quarks: 80 GeV $< m^* < 460$ GeV from $q^* \rightarrow q\gamma$, 150 GeV $< m^* < 530$ GeV from $q^* \rightarrow qW$ [21-25]. The D0 Collaboration has performed a search for excited quarks and excludes the mass range 200 GeV $< m^* < 720$ GeV [21-26]. Combining the all channels, CDF excludes the range 200 GeV $< m^* < 760$ GeV [21-27]. These exclusions are for the couplings $f = f' = f_s = 1$. Since the mass limit is sensitive to the choice of couplings, the excluded regions decrease slightly for smaller couplings.

21.3.1 The widths of excited quarks

An excited quark decays to a light quark and a gauge boson through the effective lagrangian above. Assuming $m^* > m_{W, Z}$ and neglecting ordinary quark masses, the partial decay widths for the various electroweak and QCD channels are ($V = W, Z$):

$$\Gamma(q^* \rightarrow qV) = \frac{1}{32\pi} g_V^2 f_V^2 \frac{m^{*3}}{\Lambda^2} \left(1 - \frac{m_V^2}{m^{*2}} \right)^2 \left(2 + \frac{m_V^2}{m^{*2}} \right),$$

$$\Gamma(q^* \rightarrow q\gamma) = \frac{1}{4} \alpha f_\gamma^2 \frac{m^{*3}}{\Lambda^2}, \text{ and } \Gamma(q^* \rightarrow qg) = \frac{1}{3} \alpha_s f_s^2 \frac{m^{*3}}{\Lambda^2}$$

with $f_Z = f T_3 \cos^2 \theta_W + f' \frac{Y}{2} \sin^2 \theta_W$, $f_W = f / \sqrt{2}$ and $f_\gamma = f T_3 + f' Y / 2$, where T_3 being the third component of the weak isospin, and Y being the hypercharge of q^* . Here, $g_W = e / \sin \theta_W$ and $g_Z = g_W / \cos \theta_W$ are the Standard Model W and Z coupling constants.

Table 21-8 The total decay width, Γ , of excited quarks into ordinary quarks and gauge bosons $V = g, W, Z, \gamma$ and relative branching ratios $BR = \Gamma(q^* \rightarrow qV)/\sum_V \Gamma(q^* \rightarrow qV)$ for $f = f' = f_s = 1$.

Decay mode	$m^* = \Lambda = 1000 \text{ GeV}$		$m^* = \Lambda = 3000 \text{ GeV}$	
	$\Gamma \text{ (GeV)}$	BR	$\Gamma \text{ (GeV)}$	BR
$d^* \rightarrow all$	37.3	1.0	102.	1.0
$d^* \rightarrow dg$	30.9	0.827	82.4	0.806
$d^* \rightarrow uW$	4.26	0.114	13.1	0.128
$d^* \rightarrow dZ$	1.98	0.0529	6.07	0.059
$d^* \rightarrow d\gamma$	0.22	0.0059	0.673	0.00666
$u^* \rightarrow all$	37.3	1.0	102.1	1.0
$u^* \rightarrow ug$	30.9	0.8267	82.4	0.806
$u^* \rightarrow dW$	4.26	0.114	13.01	0.128
$u^* \rightarrow uZ$	1.32	0.0353	4.05	0.0397
$u^* \rightarrow u\gamma$	0.87	0.0236	2.69	0.0264

The widths of an excited quarks decaying into a jet and a photon are small compared to the total widths as shown in Table 21-8. The total decay widths for the excited quarks (u^*, d^*) approximately 37 GeV and 102 GeV if the masses are set to $m^* = \Lambda = 1 \text{ TeV}$ and $m^* = \Lambda = 3 \text{ TeV}$, respectively. Here, it is assumed that excited quarks (u^*, d^*) are degenerate in mass and the compositeness scale is chosen to be $\Lambda = m^*$. The total width is less than the di-jet mass resolution of ATLAS (See Chapter 9.3).

21.3.2 Simulation of the signal and backgrounds

The simulation of the excited quark signal (photon+jet) and relevant backgrounds was performed with ATLFEST [21-12]. Jets are formed within a cone of radius $\Delta R = 0.7$ and required to have transverse energy $E_T > 15 \text{ GeV}$. Photons are considered isolated if they are separated from other jets by $\Delta R > 0.4$ and have maximum transverse energy $E_T < 10 \text{ GeV}$ deposition in cells in a cone $\Delta R = 0.2$ around the photon in $\eta - \phi$ space.

The processes $ug \rightarrow u^* \rightarrow u\gamma$, and $dg \rightarrow d^* \rightarrow d\gamma$ are considered. The main backgrounds from prompt photon production are given by the processes $q_i g \rightarrow q_i \gamma$, $q_i \bar{q}_i \rightarrow g\gamma$, $gg \rightarrow g\gamma$ which are referred to as background I. Backgrounds from single production of W/Z are given by $q_i \bar{q}_i \rightarrow Z\gamma$, $q_i \bar{q}_j \rightarrow W\gamma$ are referred to as background II.

The signal appears as a peak in the photon+jet invariant mass $m_{\gamma j}$. The partonic level information from PYTHIA-5.7 [21-11] for the decay products of excited quarks are shown in Figure 21-9 and Figure 21-10. The production cross sections times branching ratios for different coupling and mass of excited quarks are given in the Table 21-9. Hereafter, the cross section times branching ratio of the process is defined by σ . Photons and jets have sufficiently high transverse momenta and they are emitted predominantly in the barrel region, see Figure 21-10. The jet and photon are required to have $p_T^{\gamma, j} > 100 \text{ GeV}$ in the pseudorapidity range $|\eta^{\gamma, j}| < 2.5$. These cuts have approximately 30% acceptance.

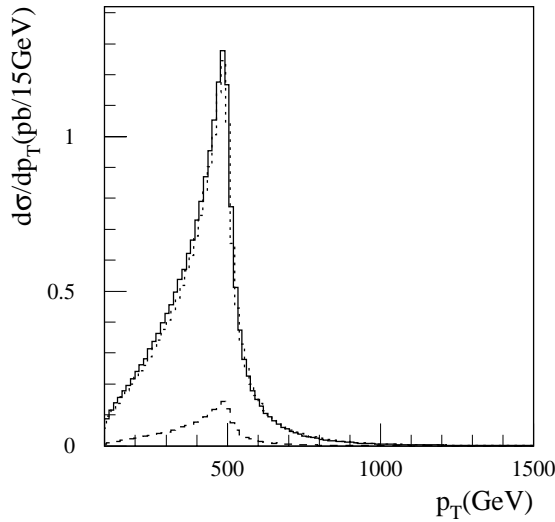


Figure 21-9 Transverse momentum distributions for excited quark signal with the scale $\Lambda = m^* = 1$ TeV and coupling $f = f' = f_s = 1$. Solid line denotes photon distributions while dotted and dashed lines are for u -quark and d -quark distributions, respectively.

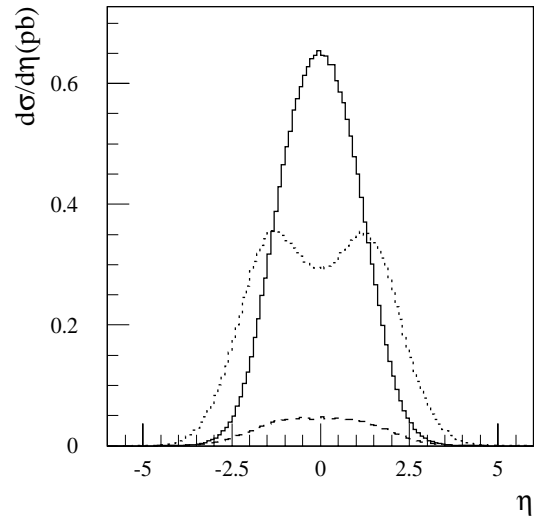


Figure 21-10 Pseudorapidity distributions for excited quark signal with the scale $\Lambda = m^* = 1$ TeV and coupling $f = f' = f_s = 1$. Solid line denotes photon distributions while dotted and dashed lines are for u -quark and d -quark distributions, respectively.

The main background is a prompt photon production associated with an energetic jet.

Table 21-9 The cross section times branching ratios, $\sigma(pb)$, for the signal at parton level are generated by PYTHIA-5.7. The values are given for the scale $\Lambda = m^*$ and the couplings for $f = f' = f_s$.

f	$m^* = 1000 \text{ GeV}$	$m^* = 3000 \text{ GeV}$	$m^* = 5000 \text{ GeV}$
1.0	21.34	7.544×10^{-2}	1.335×10^{-3}
0.5	5.373	1.933×10^{-2}	3.334×10^{-4}
0.1	2.143×10^{-1}	8.303×10^{-3}	1.340×10^{-5}
0.05	5.352×10^{-2}	1.936×10^{-4}	3.361×10^{-6}
0.01	2.144×10^{-3}	7.747×10^{-6}	1.338×10^{-7}

Figure 21-11 and Figure 21-12 show the photon+jet invariant mass distribution for the backgrounds as well as the signal at different mass values and couplings

In order to evaluate the signal significance, the photon+jet invariant mass distribution is integrated around the excited quark masses. The bin width $\Delta m_{\gamma j}$ over which the integration is performed varies as the peak of the signal widens and is taken to be $\Delta m_{\gamma j} = 135 \text{ GeV} - \Delta m_{\gamma j} = 690 \text{ GeV}$ for excited quark masses 1-6 TeV. In Table 21-10, we give the partial cross sections times branching ratios $\Delta\sigma$ for both signal, with the coupling parameters $f = f' = f_s = 1$, and the background. For smaller coupling parameters the bin width remains the same. We find an optimal cut on transverse momentum of the jets and photons, $p_T > 300 \text{ GeV}$ for the excited quark mass range 1-2 TeV, and $p_T > 1000 \text{ GeV}$ for the mass range 3-5 TeV. In

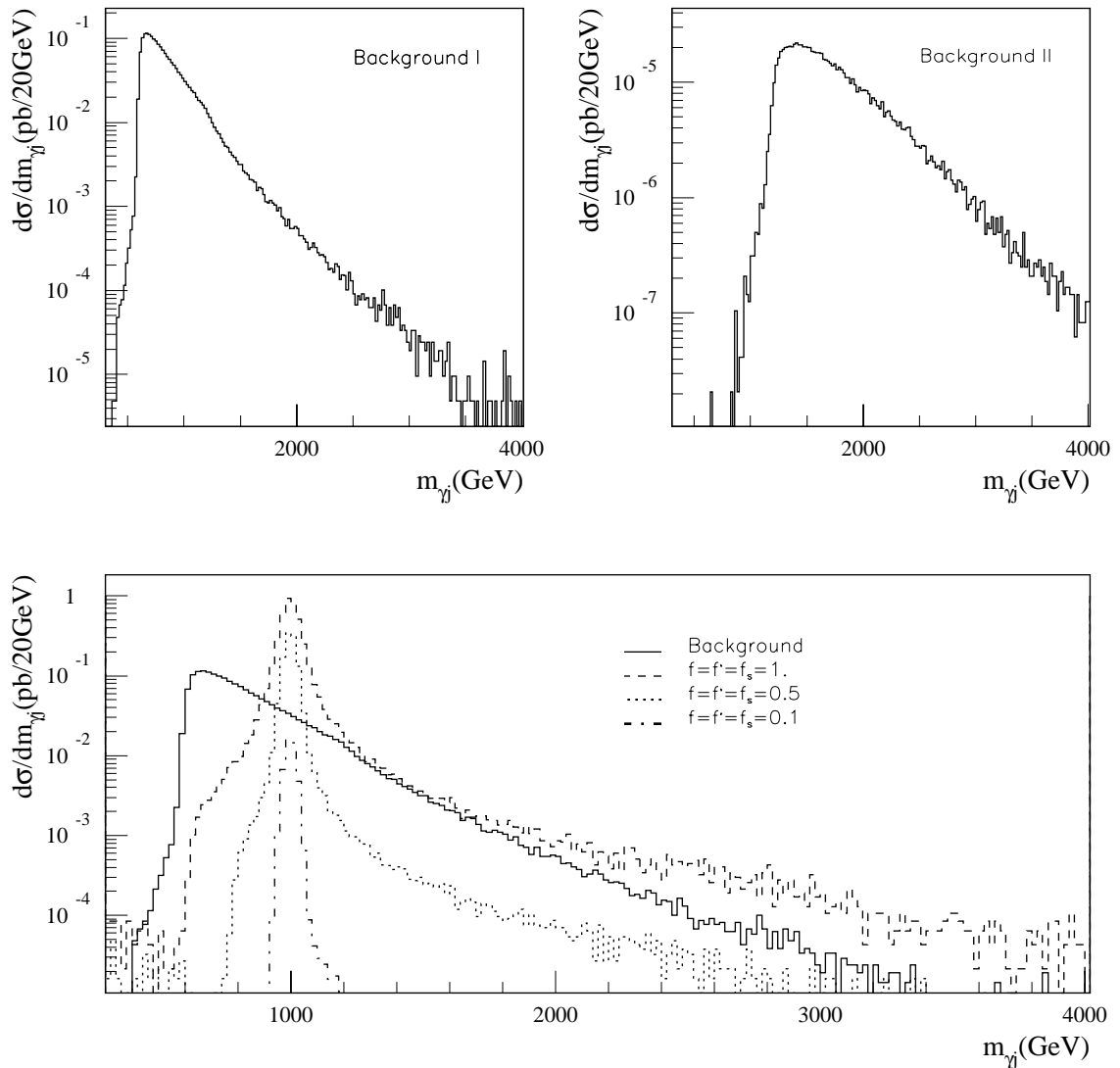


Figure 21-11 Invariant mass distributions for the excited quark signal, and backgrounds with the cuts $p_T > 300$ GeV, $|\eta| < 2.5$ for excited quark mass $m^* = 1000$ GeV. Upper figures show signal and background separately.

Figure 21-13, the expected $q^* \rightarrow q\gamma$ signal significances are defined for each mass point as S/\sqrt{B} where S and B being the number of accepted signal and background events in the chosen mass bin for an integrated luminosity of 300 fb^{-1} at LHC.

Achievable mass limits for different coupling values are established by requiring at least 10 signal events and at least 5 standard deviation significance. The discovery reach for the excited quarks at LHC are presented in Figure 21-14 For a coupling $f = f' = f_s = 1$, it is possible to reach up to $m^* = 6.5$ TeV.

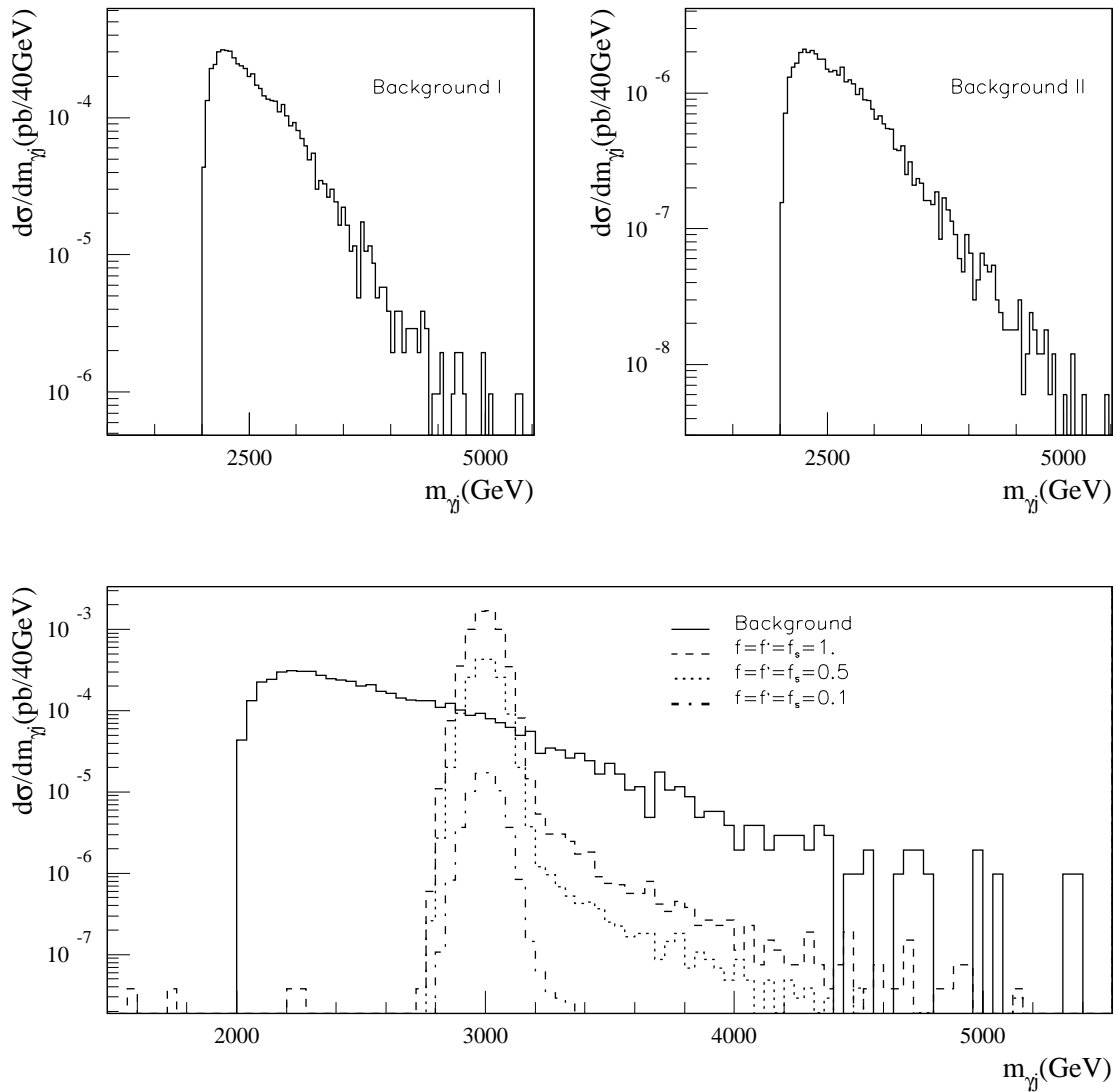


Figure 21-12 Invariant mass distributions for the excited quark signal, and backgrounds with the cuts $p_T > 1000$ GeV, $|\eta| < 1.5$ for the mass $m^* = 3000$ GeV. The upper figures show the background, the lower the signal and background combined

21.3.3 Conclusion

In conclusion, excited quarks are produced with large cross section at LHC. The results are presented for a complete analysis of the excited quark q^* production within the context of a composite model. The signal for d^* production and electromagnetic deexcitation is roughly a factor 8 smaller than for u^* . The excited quark signal (gamma+jet) was found to be dominant over prompt photon production background for the masses greater than 500 GeV. Both signal and background in the photon+jet invariant mass distribution are less by $O(\alpha/\alpha_s)$ relative to their values in the two-jet invariant mass distribution [21-27], but the signal(S)/background(B) ratio would be better in the photon+jet channel.

Table 21-10 Partial cross sections times branching ratios $\Delta\sigma$ for the signal and background are given for the bin width around the excited quark mass peak (within $\pm 2\sigma_m$). The couplings are assumed $f = f' = f_s = 1$, and transverse momentum and pseudorapidity cuts are applied for the optimisation.

m^* (GeV)	Δm_{ij} (GeV)	$\Delta\sigma^{signal}$ (pb)	$\Delta\sigma^{backg}$ (pb)
1000	135	3.552	2.312×10^{-1}
2000	255	1.245×10^{-1}	6.951×10^{-3}
3000	355	1.072×10^{-2}	6.125×10^{-4}
4000	490	1.285×10^{-3}	3.452×10^{-5}
5000	590	1.730×10^{-4}	7.553×10^{-6}
6000	690	2.414×10^{-5}	1.425×10^{-7}

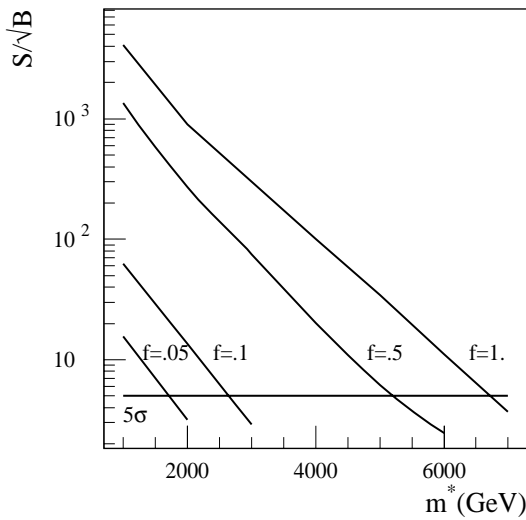


Figure 21-13 Excited quark signal significance for an integrated luminosity of 300 fb^{-1} .

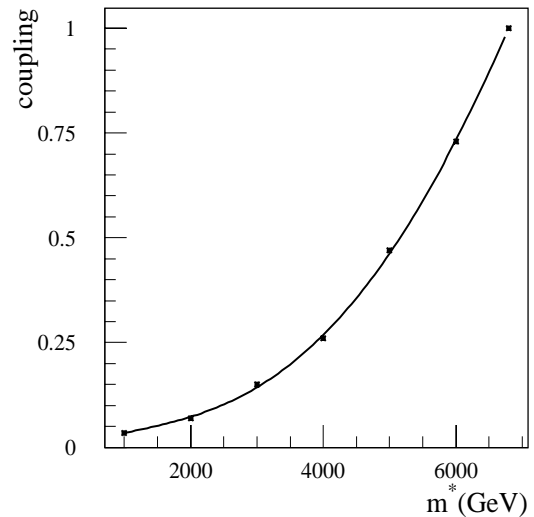


Figure 21-14 Excited quark discovery reach for an integrated luminosity of 300 fb^{-1} .

21.4 Leptoquarks

Leptoquarks (LQ s) are predicted in many extensions to the Standard Model, inspired by the symmetry between the quark and lepton generations [21-28]. These particles carry both lepton and baryon quantum numbers and hence couple to both leptons and quarks. Moreover, each fermion generation is associated with a different LQ . The various quantum numbers which characterise a given LQ are model-dependent, which precludes unique predictions of their properties.

This study considers only a scalar LQ of mass larger than 300 GeV and of charge $Q=+2/3$ or $Q=-1/3$, which couple only to the first fermion generation. LQ s of mass less than this will be observed before LHC data taking begins. The parameter k which defines the coupling at the lep-

ton-quark- LQ vertex, is assumed to be unity [21-29]). Single LQ [21-30] production and LQ pair-production [21-31] have both been studied. Studies have concentrated on the search for a first-generation LQ , assumed to decay ‘democratically’ 50% of the time to electron+jet.

Single LQ production proceeds via $q + g \rightarrow LQ + l$, where l is either an electron or a neutrino. In 25% of the cases, the final state will then consist of two electrons and one jet. The dominant background arises from Z +jets and top quark production. To minimise these backgrounds, the event selection required two electrons and one jet reconstructed with $p_T > 300$ GeV and within $|\eta| \leq 2.5$. An additional requirement that the dilepton invariant mass be larger than 120 GeV completely eliminates the Z +jet background.

Leptoquark pair production proceeds dominantly through gluon-gluon fusion, which does not involve any lepton-quark- LQ vertex and therefore is independent of the parameter k discussed above. In 25% of the events, the final state contains two electrons and two jets. The dominant background in this case is also from top pair production. It was reduced to a negligible level by requiring two electrons and two jets with $p_T > 200$ GeV and $|\eta| \leq 2.5$. In these events, both LQ masses were reconstructed above a small combinatorial background. After these cuts, the mass resolution is 27 GeV for $m_{LQ} = 1$ TeV and increases to 38 GeV for $m_{LQ} = 1.5$ TeV. Figure 21-15 shows the expected mass distribution for $m_{LQ} = 1$ TeV above the residual background which is due to top pair production. The limit of sensitivity is around 1.5 TeV.

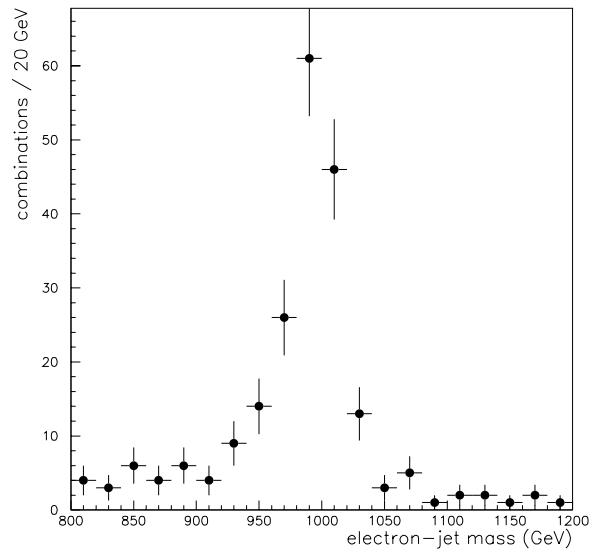


Figure 21-15 >The reconstructed electron+jet invariant mass distribution from pair production of LQ for 100 fb^{-1} .

21.5 Compositeness

21.5.1 High- p_T jets

The observation of deviations from QCD predictions of jet rates will reveal new physics such as quark compositeness, the existence of axigluons or other new particles. Measuring the inclusive jet cross section and studying the di-jet mass spectrum and angular distributions are essential tests of QCD; see Chapter 15. The existence of a quark substructure would appear as an excess of high p_T jets compared to that predicted by QCD or as di-jet angular distributions that are more isotropic than that expected in a point-like quark theory. Di-jet angular distributions have been studied by the CDF [21-32] and D0 [21-33] experiments at a centre-of-mass (CM) energy of 1.8 TeV. The highest E_T reached so far at the Tevatron, 440 GeV, corresponds to a distance scale

of order 10^{-19}m . No evidence of quark substructure was found. Previous studies of the di-jet invariant mass spectrum reported by UA1 [21-34], UA2 [21-35] and by CDF [21-36] have also shown that data that were consistent with QCD predictions.

The effect of quark compositeness at the LHC is investigated in this section. To simulate a scenario with quark substructure the event generator PYTHIA-5.7 [21-11] has been used. More details can be found in [21-37]. A simple phenomenological approach is used. This adds contact interactions between quark constituents with a compositeness scale Λ [21-38], where the sign of the effective Lagrangian for a flavour diagonal definite chirality current is positive (destructive interference) or negative (constructive interference). The data simulated in the framework of the *Standard Model* (SM) are compared with those obtained assuming quark compositeness. The simulated event sample included the following hard-scattering final states: qq , qg , gg , $g\gamma$, $q\gamma$, and $\gamma\gamma$. The γ^*/Z , W , and $t\bar{t}$ production subprocesses were also enabled. A cut on the transverse momentum of the hard scattering subprocess was set to 600 GeV. Under these conditions, the contributions from the qq , qg and gg processes represent 97% of the cross-section. For the Q^2 scale in the hard scattering $2\rightarrow 2$ process, $Q^2 = (m_{T1}^2 + m_{T2}^2)/2$ was used. Jets were reconstructed using ATLFast with a cone size $\Delta R = 0.7$. All calorimeter cells with $E_T > 1.5$ GeV are taken as possible initiators of clusters. The total E_T summed over all cells in a cone ΔR should be larger than 15 GeV. Jets were reconstructed down to $|\eta| = 5.0$.

21.5.2 Transverse energy distributions of jets.

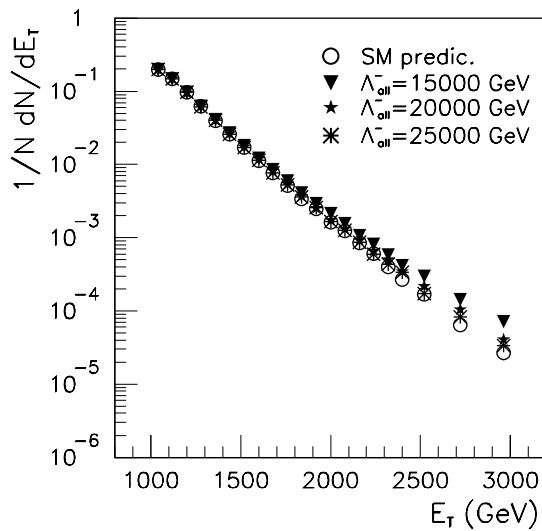


Figure 21-16 E_T distribution for two leading jets showing the Standard model prediction (open circles) and the effect of quark compositeness to the scales indicated. 30 fb^{-1} of integrated luminosity assumed.

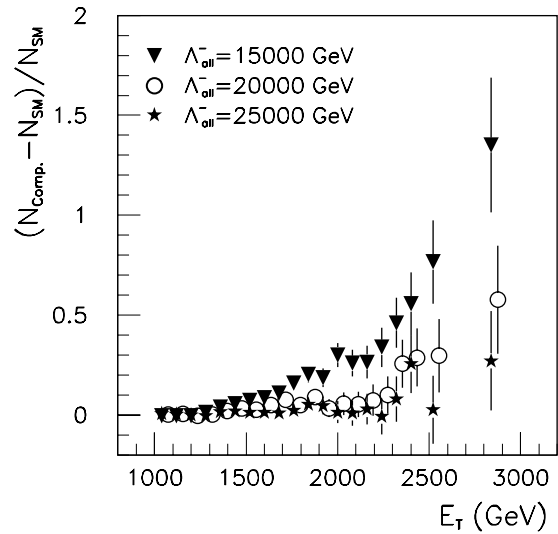


Figure 21-17 Difference of the standard model prediction and the effect of compositeness on the jet E_T distribution, normalised to the Standard Model rate. The errors correspond to 30 fb^{-1}

Figure 21-16 and Figure 21-17 show the effect of compositeness on the inclusive jet energy spectrum. The case of constructive interference is shown; the destructive case is similar. Only events with two jets of $E_T > 400$ GeV are included. Figure 21-17 shows the deviation from the Standard

Model prediction assuming that all quarks are composite. This figure emphasises that the deviation is significant only for the largest values of E_T . Figure 21-18 and Figure 21-19 show the effects on the jet E_T distribution for 300 fb^{-1} of integrated luminosity and larger values of Λ .

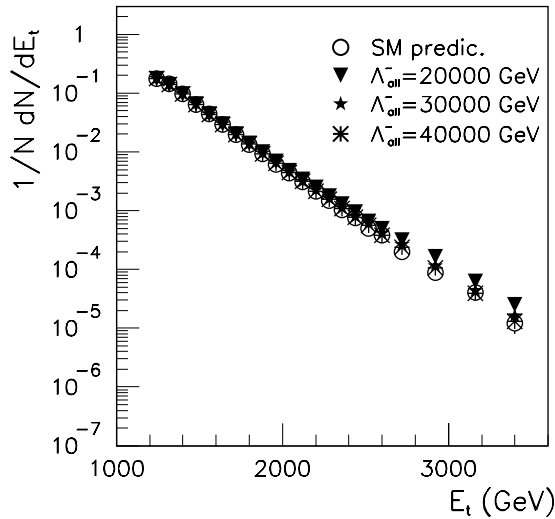


Figure 21-18 E_T distribution for two leading jets showing the Standard Model prediction (open circles) and the effect of quark compositeness to the scales indicated. 300 fb^{-1} of integrated luminosity assumed.

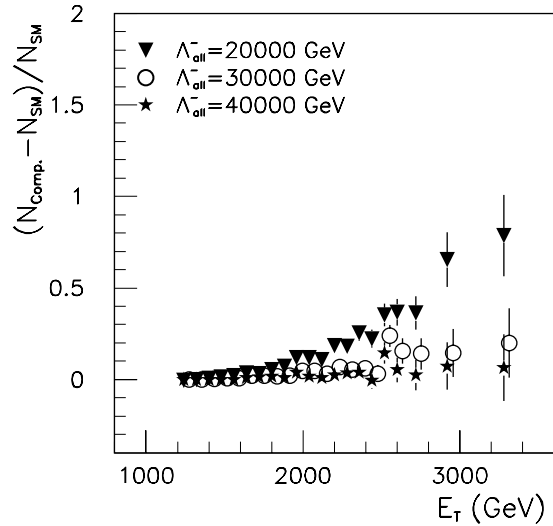


Figure 21-19 Difference of the Standard Model prediction and the effect of compositeness on the jet E_T distribution, normalised to the Standard model rate. The errors correspond to 300 fb^{-1} .

The effects of compositeness could be masked by uncertainties in the parton distribution functions (pdf's). Figure 21-20 shows a band corresponding to the results obtained with all the pdf's in PYTHIA 5.7 (except for DO1 and EHLQ1 which have large inconsistencies with present data, see also Figure 15-23). This figure should be compared to Figure 21-18. While the differences shown here are comparable to the effects of compositeness for $\Lambda > 15000 \text{ GeV}$, the allowed range of pdf's will be further constrained by the time that LHC starts running. Furthermore, as will be shown below, the angular distributions are rather insensitive to pdf's.

The non-linear response of the hadron calorimeter can mask the true difference between the SM and a compositeness scenario, or fake a compositeness signal. To study this effect, the non-linearity of the jet E_T scale was parametrised by the relation [21-39]

$$E_T(\text{meas}) = E_T \cdot \frac{1}{c(1 + (e/h - 1) \cdot b \cdot \ln E_T)}$$

where $e/h = 1.36$ and c is adjusted such that at 500 GeV the scale is unchanged. The parameter b controls the size of the non-linearity. After correction the residual uncertainty can be parametrised by this formula with $b = 0.025$ and corresponds to a 1.5% non-linearity at 3 TeV . If no correction is made then $b = 0.11$ and there is a 5% non-linearity at 3 TeV . More details can be found in Section 9.1.1.3.

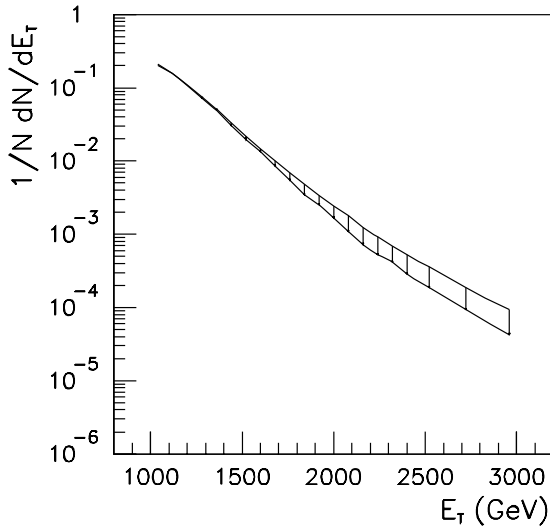


Figure 21-20 The jet E_T spectrum showing the uncertainty from present pdf's; 30 fb⁻¹ assumed.

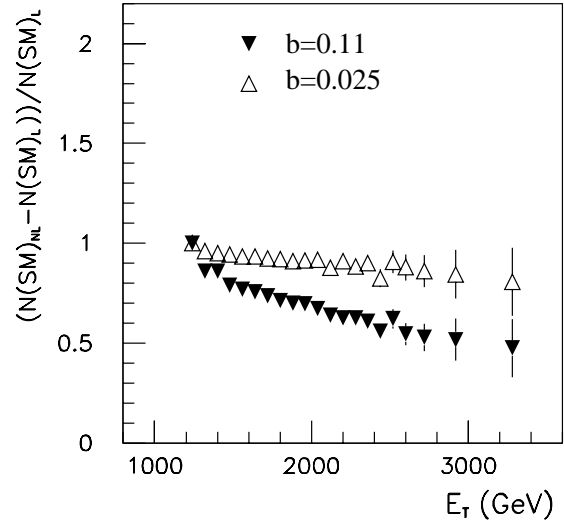


Figure 21-21 The fractional difference between the E_T spectrum measured by a linear and non-linear calorimeter. The curves are normalised at 1.25 TeV.

The effect of non-linearity shown in Figure 21-21. The figure shows the fractional deviation of the transverse energy spectrum as measured by a non-linear calorimeter to that expected from a linear one. The rates are normalised to be equal at 1.25 TeV. Two non-linearities are shown corresponding to $b = 0.025$ and $b = 0.11$. It can be seen by comparing this plot to that of Figure 21-19 that, in the worse case, the effect of a nonlinearity is similar in magnitude to that due to a composite scale of 20 TeV, and that if the 1.5% non linearity can be achieved then it is comparable to the 30 TeV case.

In order to assess the sensitivity of the E_T spectrum to the composite scale the event excess above some value of E_T is needed. If N is the number of events in the E_T spectrum, define

$$R = \left(\frac{N(E_T > E_T^0)}{N(E_T < E_T^0)} \right)_{comp} \bigg/ \left(\frac{N(E_T > E_T^0)}{N(E_T < E_T^0)} \right)_{SM}$$

With the choice $E_T^0 = 1500$ GeV one can conclude that ATLAS is sensitive at 95% confidence to values of Λ as large as 25 (40) TeV for 30 (300) fb⁻¹. If this sensitivity is to be achieved then the calorimeter non-linearity must be understood at the 1.5% level.

21.5.3 Jet angular distributions.

The angular distribution of the jets are more sensitive to compositeness signals than the jet transverse energy spectrum and less susceptible to calorimeter non-linearities. The analysis was made in terms of an angular variable $\chi \equiv e^{|\eta_1 - \eta_2|}$, where $\eta_{1,2}$ are the pseudorapidities of the two leading jets. For the case of 2→2 parton scattering, it is related to the CM scattering angle Θ^* as follows:

$$\chi = \frac{1 + |\cos \Theta^*|}{1 - |\cos \Theta^*|}.$$

The di-jet angular distribution, $(1/N)(dN/d\chi)$, was investigated in four di-jet invariant mass bins. For all di-jet invariant mass bins, the E_T -threshold for the highest E_T jet was 400 GeV. Table 21-11 shows the selection cuts for the highest E_T jet for the various invariant di-jet mass bins, to-

Table 21-11 Characteristics of the invariant mass of the high E_T jets.

Mass bin (GeV)	2000-2300	23-00-2800	2800-3400	>3400
E_T threshold(GeV)	400	400	400	400
No of events	18 562	15 781	7772	5228
Average m_{jj} (GeV)	2136	2512	3050	4048

gether with the average M_{jj} and the number of events per bin . The di-jet angular distributions for these di-jet mass bins are shown in Figure 21-22 for constructive interference. The destructive interference case is very similar [21-37]. From the figure, one can see that quark compositeness leads to an enhancement in the distribution at low values of χ in comparison to the SM prediction. The di-jet mass range above 3400 GeV is shows clearly the isotropic contributions to the di-jet angular distribution in pp interactions at LHC for Λ up to 8 TeV. The sensitivity is slightly greater for a constructive interference than for a destructive one.

Define R_χ as the fraction of events with $\chi > \xi_0$. In Figure 21-23 the dependence of R_χ on the scale Λ , is shown for the constructive and destructive cases, when either two or all quarks are composite; $\xi_0 = 5$ was used. It is clear, that there is not enough sensitivity to distinguish whether two or all quarks are composite.

R_χ is not very sensitive to the parton density function as illustrated in Figure 21-24, where the values of R_χ are shown for the mass bin of M_{jj} above 3400 GeV. These predictions have been obtained for the cases when two or all quarks are composite. R_χ is also insensitive to the jet cone radius ΔR . Note that in the rest of the analysis, PYTHIA was used with the default structure function CTEQ2.

To study the sensitivity to the quark compositeness signal for higher scale Λ , an analysis was performed for an integrated luminosities of 30 fb^{-1} and 300 fb^{-1} . Figure 21-25 and Figure 21-26 show the deviation of the di-jet angular distribution from the Standard Model predictions.

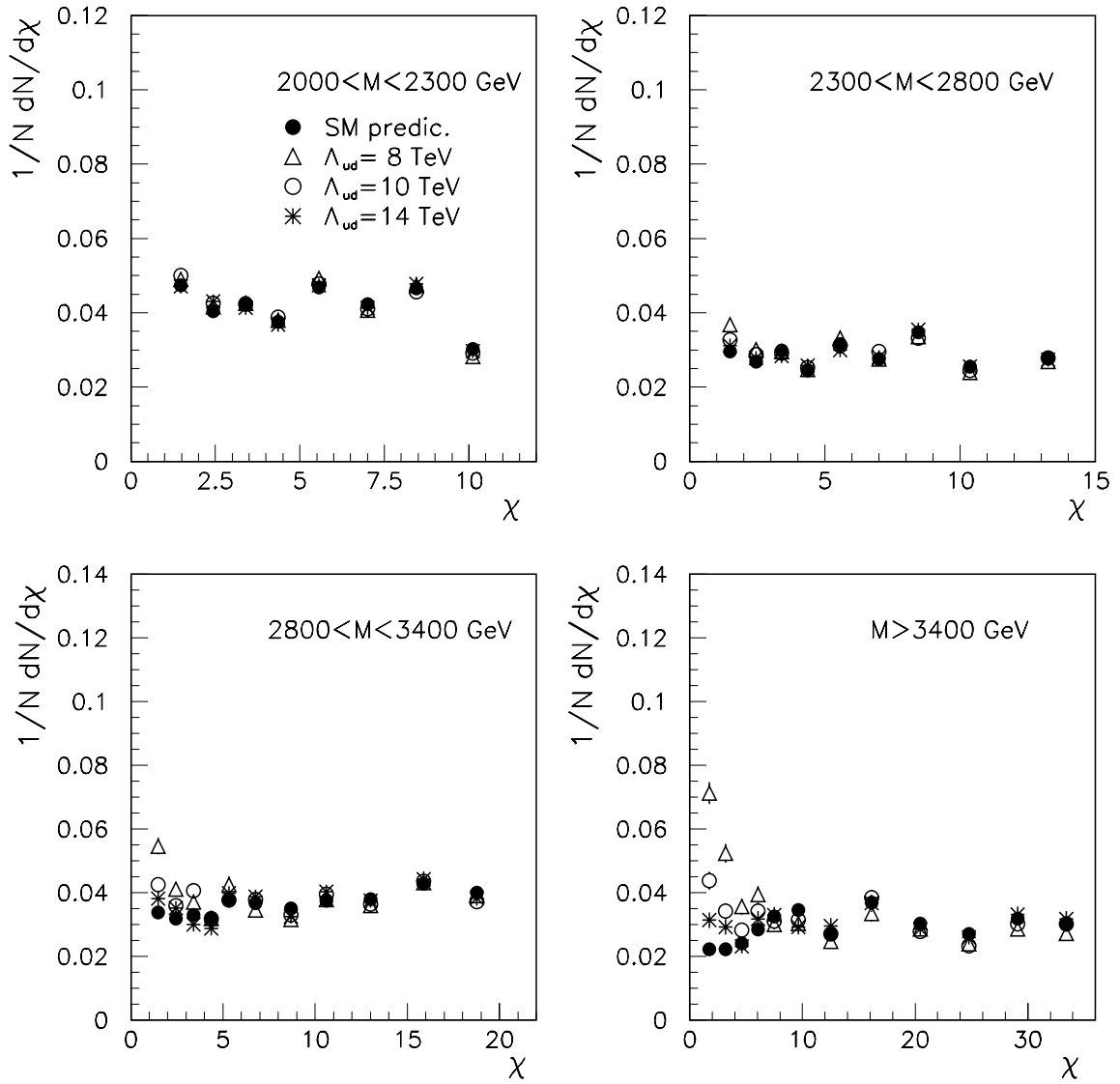


Figure 21-22 Di-jet angular distributions for various mass bins in case of constructive interference. Only quarks of the first two generations are assumed to be composite. The compositeness scale is taken to be 8, 10 and 14 TeV.

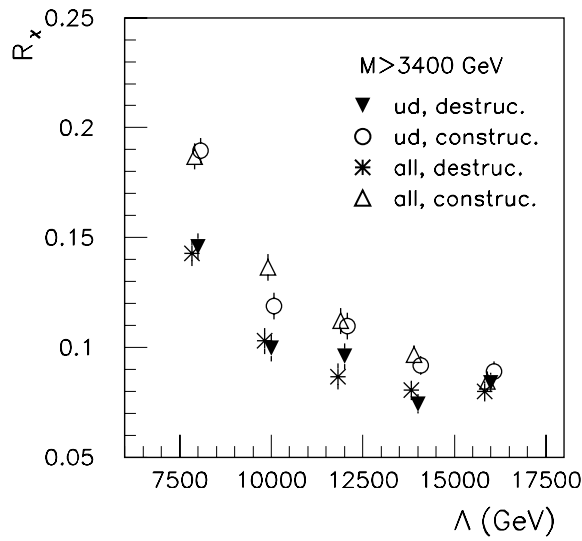


Figure 21-23 The dependence of R_χ on the scale Λ , for the constructive and destructive cases, when two or all quarks are composite.

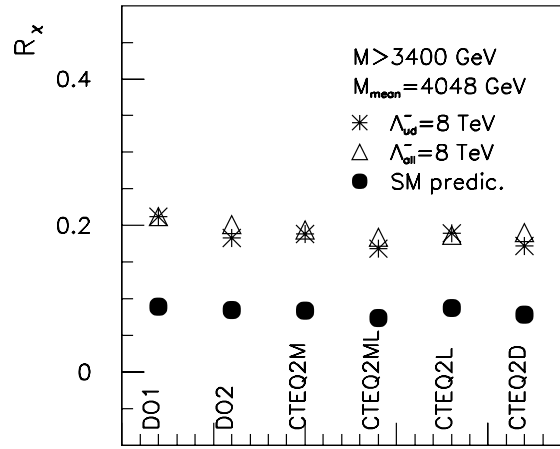


Figure 21-24 The dependence of R_χ on the parton density function.

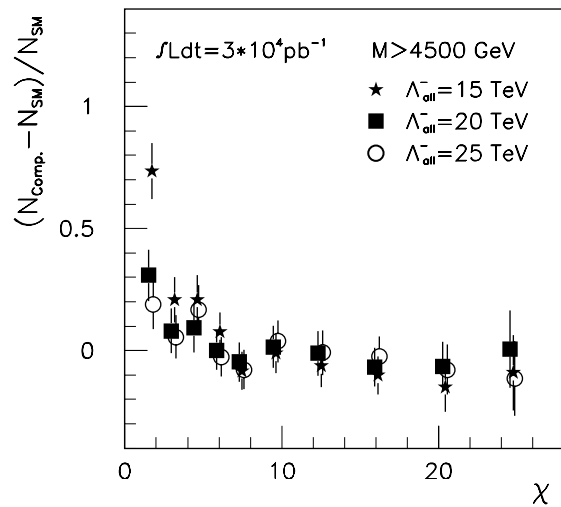


Figure 21-25 The di-jet angular distribution for di-jet mass above 4500 GeV for 30 fb^{-1} .

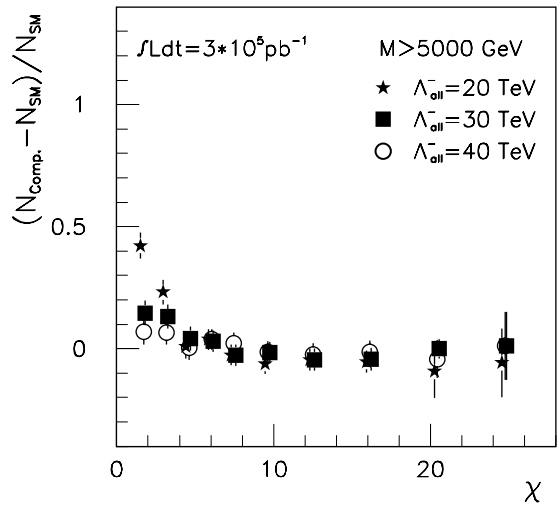


Figure 21-26 The di-jet angular distribution for di-jet mass above 5000 GeV for 300 fb^{-1} .

The sensitivity of the angular distributions to the calorimeter resolution has been studied [21-40]. In order to investigate the influence of a change of the constant term in the jet energy resolution on $(1/N)(dN/d\chi)$. The constant term was varied by a factor of two. There is no significant impact on the di-jet angular distribution. Figure 21-27 compares the SM and composite quarks predictions with and without non-linearity effects. Both non-linearities discussed above are shown on the figure. Even for the larger of these, the effect is negligible compared to the compositeness signal shown. For this choice of di-jet mass bin intervals and jet E_T , no fake signal is created and that the angular distribution is quite insensitive to the non-linearity.

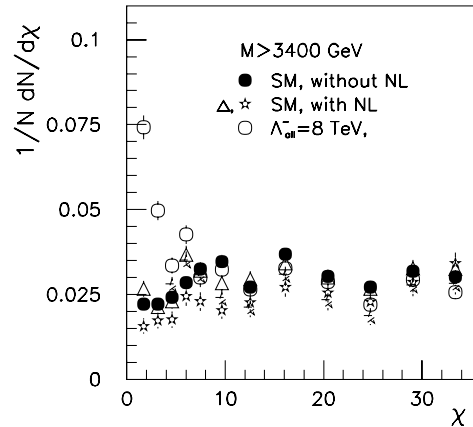


Figure 21-27 The jet angular distributions showing the effects of non-linearity.

In conclusion, the study shows that high mass di-jet angular distribution has an excellent discovery capability for quark compositeness. One month of LHC operation at $10^{33} \text{ cm}^{-2}\text{s}^{-1}$ allows discovering quark substructure if the constituent interaction constant is of the order of 14 TeV. An integrated luminosity of 300 fb^{-1} is needed to reach a 95% CL limit of 40 TeV.

21.5.4 Dilepton production

The production of dilepton pairs of large invariant mass can be used to probe models where leptons and quarks share constituents [21-38]. Events are selected with two isolated leptons of the same flavour and opposite charge, with $p_T > 400 \text{ GeV}$ and $|\eta| < 2.5$. The Standard Model rate is dominated by Drell-Yan pairs. A composite signal is revealed by an excess of events at large lepton pair invariant mass. If the invariant mass is greater than 1 TeV, the Standard model predicts a rate of 7 fb and the presence of compositeness with $\Lambda = 16 \text{ TeV}$ increases this by 6 fb. For an integrated luminosity of 100 fb^{-1} , a sensitivity to $\Lambda < 30 \text{ TeV}$ is achievable at the 5σ level. Details can be found in [21-41].

21.6 Search for new gauge bosons and Majorana neutrinos

New gauge bosons arise from extensions of the Standard Model gauge group and are thus related to the generators of new symmetry groups [21-42]. Given the large number of possible models, a complete survey is not possible. Therefore, in the first part of this section, the discovery potential for new neutral and charged bosons (further referred to as Z' and W' respectively) will be reviewed. To do so, the prescriptions of a reference model [21-43], in which the couplings of W' and Z' to quarks and leptons are the same as for the standard W and Z bosons, and the $W'WZ$ and $Z'WW$ are suppressed by a factors of $(m(W)/m(W'))^2$ and $(m(Z)/m(Z'))^2$, will be followed.

In order to illustrate the capability for revealing the exact nature of new bosons, a detailed study was also performed in the framework of the Left-Right Symmetric Model, and is presented here.

21.6.1 Search for new vector bosons

21.6.1.1 Fermionic decays of Z' bosons

If the couplings of a new Z' boson to quarks and leptons are the same as those of a Standard Model Z boson and there is no significant Z - Z' mixing, then the decay width of the Z' boson grows linearly with its mass. This situation, which is probably the most favourable case, will be further referred to as a SM-like Z' . The discovery limits in the e^+e^- , $\mu^+\mu^-$ and jet-jet (jj) decay channels as a function of $m(Z')$ are presented in Figure 21-28 [21-44]. The jets are required to have p_T greater than 300 GeV. Shown is the value of σ_B for the Z' relative to the value for a Standard Model Z , that is needed for a 5σ confidence level signal as a function of the mass of the Z' . As anticipated, the best sensitivity is obtained in the e^+e^- channel. The other decay channels, together with the measurement of the forward-backward asymmetry, are likely to provide some complementary information which are relevant to determine the couplings of the fermions to the Z' boson and to thereby help in specifying the origin of a new resonance. In the jj final state the signal to background ratio is rather small (between 10^{-3} and 10^{-2}), but a peak is visible [21-44].

21.6.1.2 Leptonic decays of W' bosons

Within the same model, the sensitivity to a possible signal from leptonic W' decays extends to masses of about 6 TeV [21-45]. For a value of $m(W') = 4$ TeV, Figure 21-29 shows the expected electron-neutrino transverse mass distribution for the signal above the dominant background from $W \rightarrow e\nu$ decays. For a transverse mass above 2.3 TeV and an integrated luminosity of 100 fb^{-1} , a clean signal of 160 events is expected above a background of 13 events from $W \rightarrow e\nu$ decays and a negligible contribution from top quark pair production and decay. With such a signal sample, the W' mass could be measured to an accuracy of about 50 GeV.

21.6.1.3 A study of $W' \rightarrow WZ$

In addition to the leptonic channels, a new W' charged boson could be observed via its decay into a WZ pair. Here, the three lepton decay channel $W' \rightarrow WZ \rightarrow (lv)(ll)$ is considered for the mass range of W' from 500 GeV up to 3 TeV. To obtain the W' signal, the transverse mass distribution of three leptons and missing E_T is calculated. From the three leptons in the final state, the ones with opposite charges are paired in order to reconstruct the Z boson (when there are two possibilities, only the pair for which the invariant mass is the closer to $m(Z)$ is selected). The transverse mass distribution of the remaining lepton and the missing E_T shows a Jacobian peak at $m(W)$.

The main background for this channel is the irreducible pair production and leptonic decays of W and Z gauge bosons $pp \rightarrow WZ \rightarrow (lv)(ll)$. In addition, there is a reducible background from $pp \rightarrow ZZ$ with one misidentified lepton in the final state, as well as the reducible background from $pp \rightarrow tt \rightarrow WbWb$, where both W bosons decay into a lv pair and where the third lepton comes from one of the b quarks. This background is significantly reduced when one requires three isolated leptons in the final state, since the soft lepton coming from the b quarks is non-isolated. The transverse mass distribution of the three leptons and the escaping neutrino are shown in Figure 21-30 for both the signal and the background. Even when no cut is applied, the W' signal can be seen clearly up to masses of 2.5 TeV.

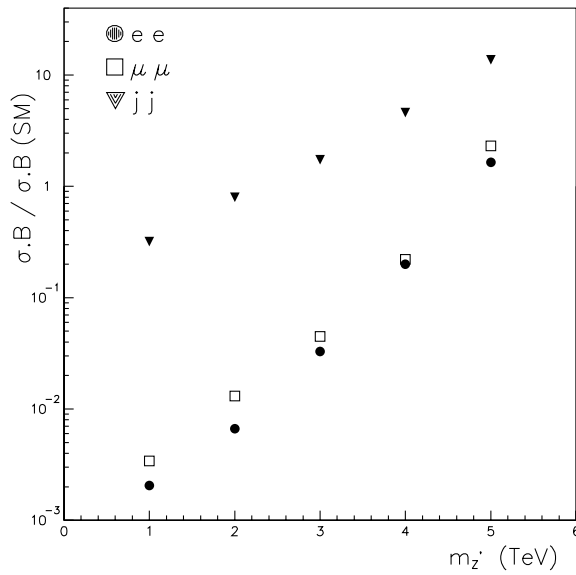


Figure 21-28 Discovery potential for a new Z' neutral boson with 100 fb^{-1} as a function of the Z' mass and the ratio of its coupling strength to that of a Standard Model Z .

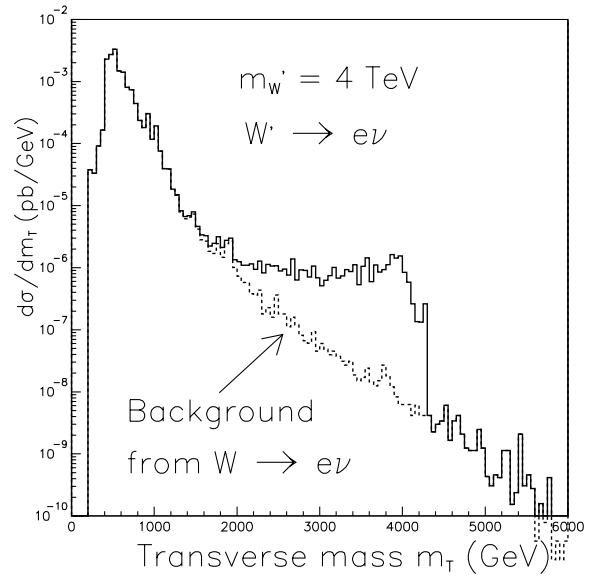


Figure 21-29 Expected transverse mass distribution for $W' \rightarrow e\nu$ decays above the dominant $W \rightarrow e\nu$ background, with $m(W') = 4 \text{ TeV}$ and for an integrated luminosity of 100 fb^{-1} .

Some additional cuts have been applied on the transverse momentum of the lepton, in order to further enhance the signal and reduce the background. The event rates and the corresponding statistical significances strongly depend on the coupling of W' to the WZ pair. In the following, a SM-like situation will be referred to when the coupling of W' to the WZ pair is equal to the Standard Model coupling of W to WZ reduced by a factor $(m(W)/m(W'))^2$: the corresponding cross section will be further denoted by $(\sigma B)_{\text{SM}}$. Table 21-12 shows the event rates for the signal and background in the three lepton final state; to the total background includes the contribution from top pair events

In order to accommodate different couplings from other possible models, the limiting value of the $W'WZ$ coupling, corresponding to a significance of 5σ after 300 fb^{-1} has been determined. The cross section associated with this discovery limit will be further denoted by $(\sigma B)_{\text{limit}}$. In Figure 21-31, the ratio of the cross section leading to a 5σ significance to the cross section calculated with SM-like coupling for the W' boson is plotted as a function of $m(W')$, in the range between 500 GeV and 3 TeV .

Table 21-12 Event rates for the signal and background for 300 fb^{-1}

$m_{W'} = 500 \text{ GeV}$		$\sigma_{\text{SM}} = 0.232 \text{ pb}$			
$m_T > 275 \text{ GeV}$	$W' \rightarrow WZ$	B_{WZ}	B_{ZZ}	B_{total}	S/\sqrt{B}
no cut	25446	5368	535	28736 *	150.1
$m_Z \mp 3\Gamma$					
$p_{Tl,\nu} > 50 \text{ GeV}$	7884	341	16	357	417.4
$p_{TZ} > 200 \text{ GeV}$					
$m_{W'} = 1000 \text{ GeV}$		$\sigma_{\text{SM}} = 1.506 \cdot 10^{-2} \text{ pb}$			

* Including $t\bar{t}$ background

Table 21-12 Event rates for the signal and background for 300 fb⁻¹

$m_{W'} = 500 \text{ GeV}$		$\sigma_{\text{SM}} = 0.232 \text{ pb}$			
$m_T > 495 \text{ GeV}$	$W' \rightarrow WZ$	B_{WZ}	B_{ZZ}	B_{total}	S/\sqrt{B}
no cut	1826	714	77	1552 *	46.4
$m_Z \mp 3\Gamma$					
$p_{T l,\nu} > 50 \text{ GeV}$	627	23	3	26	122.9
$p_{TZ} > 450 \text{ GeV}$					
$m_{W'} = 2000 \text{ GeV}$		$\sigma_{\text{SM}} = 7.099 \cdot 10^{-4} \text{ pb}$			
$m_T > 1140 \text{ GeV}$	$W' \rightarrow WZ$	B_{WZ}	B_{ZZ}	B_{total}	S/\sqrt{B}
no cut	67	20	2	22	14.28
$m_Z \mp 3\Gamma$					
$p_{T l,\nu} > 50 \text{ GeV}$	45	4	-	4	22.5
$p_{TZ} > 700 \text{ GeV}$					
$m_{W'} = 2500 \text{ GeV}$		$\sigma_{\text{SM}} = 2.498 \cdot 10^{-4} \text{ pb}$			
$m_T > 1425 \text{ GeV}$	$W' \rightarrow WZ$	B_{WZ}	B_{ZZ}	B_{total}	S/\sqrt{B}
no cut	20	6	1	7	5.66
$m_Z \mp 3\Gamma$					
$p_{T l,\nu} > 50 \text{ GeV}$	14	4	1	5	4.68
$m_{W'} = 3000 \text{ GeV}$		$\sigma_{\text{SM}} = 7.652 \cdot 10^{-5} \text{ pb}$			
$m_T > 2119 \text{ GeV}$	$W' \rightarrow WZ$	B_{WZ}	B_{ZZ}	B_{total}	S/\sqrt{B}
no cut	5	1	-	1	3.24

* Including $t\bar{t}$ background

21.6.1.4 A study of $Z' \rightarrow WW$

A similar study can be performed if a new Z' neutral boson couples to the standard W boson. To illustrate this, the $pp \rightarrow Z' \rightarrow WW \rightarrow (jj)(e\nu_e)$ is considered; the mass range of the Z' boson extends from 1 TeV to 3 TeV. To reconstruct the Z' signal, the hadronic and leptonic decays of the W bosons are treated separately.

Given the large transverse momentum of the W bosons, the two hadronic jets from their decays are very close and difficult to separate in the detector. After determining the radius ΔR_θ of the cone in which the two hadronic jets coming from the W boson are to be found, the invariant masses of all the hadronic clusters with a radius equal to ΔR_θ are calculated using the detailed calorimeter information. Note that as the mass of the Z' increases, ΔR_θ is reduced. The hadronic cluster for which the invariant mass is the closest to the value of $m(W)$ is then assigned to the hadronic W decay.

For the leptonic W boson decay, the longitudinal momentum of the neutrino can be found by using its missing transverse energy and by solving a second order equation using the W mass as a constraint. The resulting $p_z(\nu_e)$, then permits a full reconstruction of the W boson momentum.

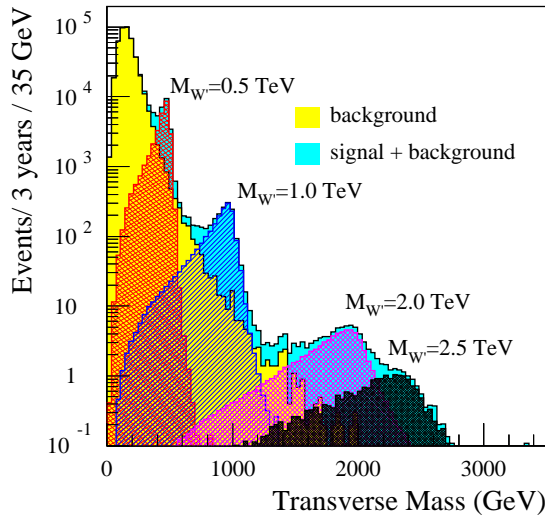


Figure 21-30 Transverse mass distribution of the three leptons and the escaping neutrino for the decay of a W boson into a WZ pair and for the corresponding background, for an integrated luminosity of 300 fb^{-1} .

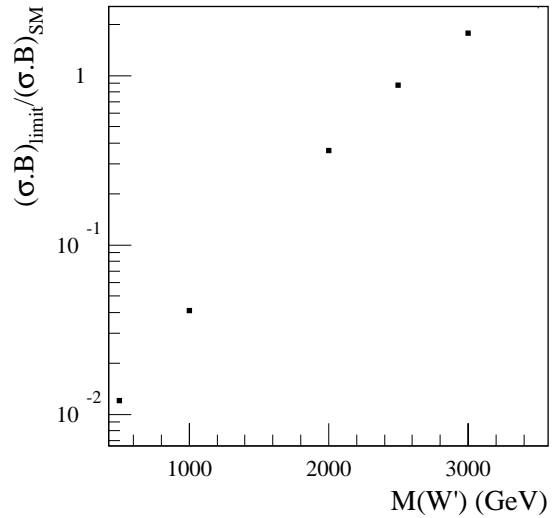


Figure 21-31 Discovery limit for a W' boson in the WZ decay channel as a function of the W' mass and the W' coupling to the WZ pair (see text), for an integrated luminosity of 300 fb^{-1} .

The major background for this channel is $pp \rightarrow W + \text{jets}$, where W decays into a $e\nu_e$ pair, while the additional jets give an invariant mass which is close to the W mass (this background depends on the value chosen for ΔR_ρ). In addition, the production of $t\bar{t}$ and WW pairs, where the W bosons have a large transverse momentum contribute. All these backgrounds can be reduced by the use of the following cuts:

- $E_T(W \rightarrow e\nu_e) > m(Z')/3$, $E_T(e) > m(Z')/10$, $E_T^{\text{miss}} > m(Z')/10$ and $m_T(e\nu_e) < 100 \text{ GeV}$.
- $E_T(W \rightarrow jj) > m(Z')/3$ and $m(W) - 15 \text{ GeV} < m_{\text{inv}}(W \rightarrow jj) < m(W) + 15 \text{ GeV}$.
- $|\eta(W \rightarrow jj)| < 2$ and $|\eta(e)| < 2$.
- A veto on the jets in the $|\eta| < 2$ region: the events for which some jets, apart from the ones coming from the W boson, have a transverse energy greater than 25 GeV are rejected (this cut is very efficient in reducing the $t\bar{t}$ background).

The reconstructed mass of the Z' boson is shown in Figure 21-32, together with the contribution from the residual background.

As in the case of the $pp \rightarrow W' \rightarrow WZ$ process, the event rates and the corresponding statistical significance strongly depend on the coupling of the new Z' neutral boson to the WW pair. Here again, a SM-like situation is referred to when the coupling of Z' to the WW pair is equal to the Standard Model coupling of the Z boson to the WW pair reduced by a factor $(m(Z)/m(Z'))^2$. As in Section 21.6.1.3, the limiting value of the Z' WW coupling, corresponding to a significance of 5σ for 300 fb^{-1} , can be determined (see Figure 21-33).

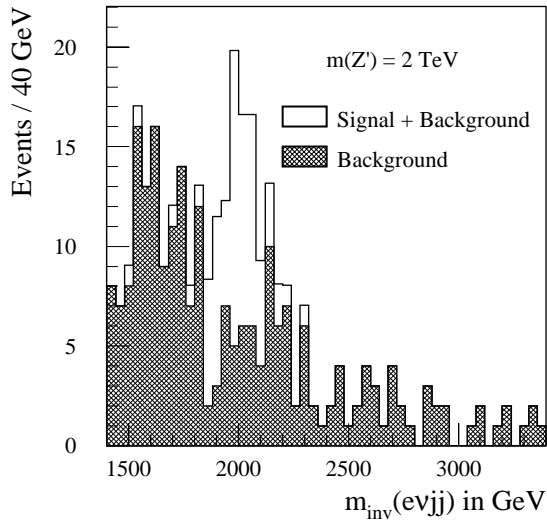


Figure 21-32 Invariant mass distribution of the two hadronic jets, the electron and the neutrino for the decay of a 2 TeV Z' boson into a WW pair and the corresponding background.

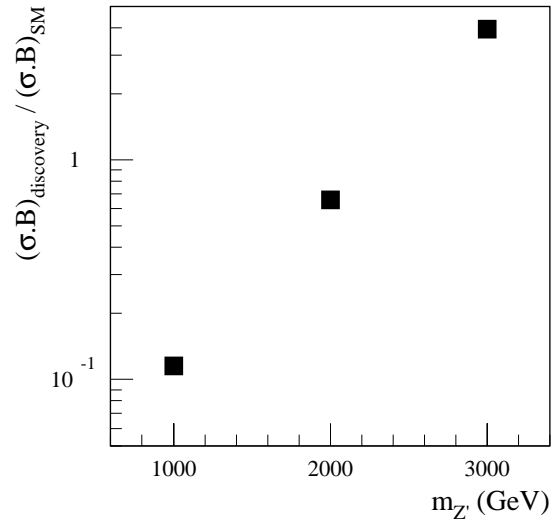


Figure 21-33 Discovery limit for a Z' boson in the WW decay channel as a function of the Z' mass and the Z coupling to the WW pair (see text), for an integrated luminosity of 300 fb^{-1} .

21.6.2 Search for right-handed Majorana neutrinos

In the Standard Model, there are no right-handed neutrinos. As a result, given the Higgs structure of the theory, neutrinos are massless particles. However, no fundamental principle forbids them from acquiring masses and extensions to the Standard Model can have right-handed massive neutrinos.

An alternative model based on the $SU(2)_R \times SU(2)_L \times U(1)_{B-L}$ gauge group, restores the parity symmetry at high energy by using isospin doublets to describe both left-handed and right-handed fermions and by introducing three new heavy gauge bosons: W_R and Z' [21-46]. If neutrinos are Majorana particles, the Left-Right Symmetric Model also provides an explanation for the lightness of the left-handed neutrinos (further referred to as ν 's) by introducing heavy right-handed neutrinos (further referred to as N 's) and using the See-Saw mechanism [21-47]. If the spontaneous breaking occurs at the TeV scale (as suggested by some supersymmetric extensions of the Left-Right Symmetric Model [21-48]), then the discovery of W_R boson and right-handed Majorana neutrinos, could be made via the process $pp \rightarrow W_R + X \rightarrow lN + X \rightarrow llqq + X$ [21-49].

PYTHIA 5.7 and JETSET 7.4 have been used in order to generate the $pp \rightarrow W_R$ events and the right-handed Majorana neutrinos have been implemented so that the decay chain above can be studied. In this study, the coupling constants and the CKM matrices are assumed to be identical for left-handed and right-handed fermions. Two extreme mass situations are considered, in which either the masses of N_e, N_μ and N_τ are equal or $m(N_e) \ll m(N_\mu)$ with both N_μ and N_τ heavier than the W_R boson. In the following, only the $N_e \rightarrow qqe$ decays will be studied in detail.

21.6.2.1 Reconstruction of W_R and N_e

Events with two isolated electrons and at least two hadronic jets in the final state are selected (the remnants of the pp collision and the gluons radiated by the quarks coming from N_e decays usually lead to a jet multiplicity which is greater than two). Then, one assumes that the two hadronic jets with highest transverse energies come from N_e . Since one does not know if a given electron comes from W_R or N_e , the two (ej_1j_2) combinations must be considered in order to reconstruct the right-handed Majorana neutrino. The W_R boson is reconstructed by calculating the invariant mass of the (eej_1j_2) system. Figure 21-34 shows the mass distributions which are obtained for the signal after these procedures.

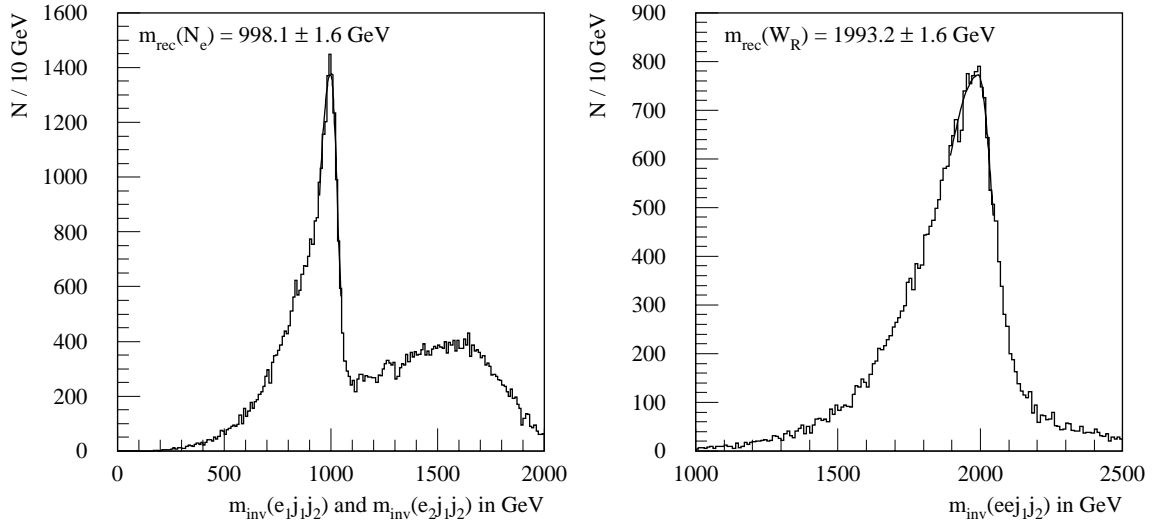


Figure 21-34 Reconstruction of N_e and W_R when their masses are respectively 1 and 2 TeV. The plots are given for an integrated luminosity of 300 fb^{-1} and when the three Majorana neutrinos are degenerate in mass. The peaks are fitted with an asymmetric Gaussian distribution.

The shape of the spectra are not symmetric, because of the final state radiation of hard gluons. As the asymmetry in the W_R and N_e mass distributions grows with $m(N_e)$, the following selection criteria will be further applied on the signal events

$$0.7m(N_e) \leq m_{inv}(e_1j_1j_2) \leq 1.1m(N_e) \quad \text{or} \quad 0.7m(N_e) \leq m_{inv}(e_2j_1j_2) \leq 1.1m(N_e)$$

$$(0.9 - 0.2r_W)m(W_R) \leq m_{inv}(eej_1j_2) \leq 1.1m(W_R)$$

where $r_W = (m(N_e))/(m(W_R))$. Note that when r_W is small, it becomes more difficult to extract a clean signal with two isolated electrons and at least two hadronic jets, since the decay products of the right-handed Majorana neutrino are very close to each other. In this case, one should look for signatures with one high- p_T isolated electron and one high- p_T hadronic jet.

21.6.2.2 Reduction of the background and discovery potential for W_R boson N_e

All the physics processes which lead to two isolated electrons and at least two hadronic jets in the final state are potential sources of background. In the framework of the Standard Model, the following processes are considered:

- $pp \rightarrow WW, WZ, ZZ (+ \text{jets}) \rightarrow ee + \text{jets}$,
- $pp \rightarrow t\bar{t} \rightarrow WWbb \rightarrow ee + \text{jets}$,
- $pp \rightarrow Z/\gamma^* (+ \text{jets}) \rightarrow ee + \text{jets}$.

The two isolated electrons produced in these processes come either from a Z boson or from a WW pair. Their transverse energy is thus rather limited. The same applies for the two selected hadronic jets. Kinematical cuts at 200 GeV and 100 GeV are thus applied on $m_{inv}(ee)$ and on the transverse energy of j_1 and j_2 . In a first step, the cuts that are used to reduce the background are $m_{inv}(ee) > 200$ GeV and $E_T(j_1 j_2) > 100$ GeV, when there are two isolated electrons and at least two hadronic jets in the final state (see full circles and squares). For events with one isolated electron and one hadronic jet which deposits a significant fraction of its energy in the electromagnetic calorimeter (see open circles and squares), one applies a kinematical cut at 1 TeV on the transverse energy of both the electron and the hadronic jet.

After 30 fb^{-1} , the $pp \rightarrow W_R \rightarrow e N_e$ channel will allow the discovery of the W_R boson and the right-handed Majorana neutrino N_e at the 5σ confidence level up to masses of 4.6 TeV and 2.8 TeV respectively (if there is no residual background in a given region of the (W_R, N_e) mass plane, one requires at least ten signal events for discovery). After 300 fb^{-1} , these discovery limits can be pushed up to 5.8 TeV for $m(W_R)$ and 3.4 TeV for $m(N_e)$, as it is shown on Figure 21-35a.

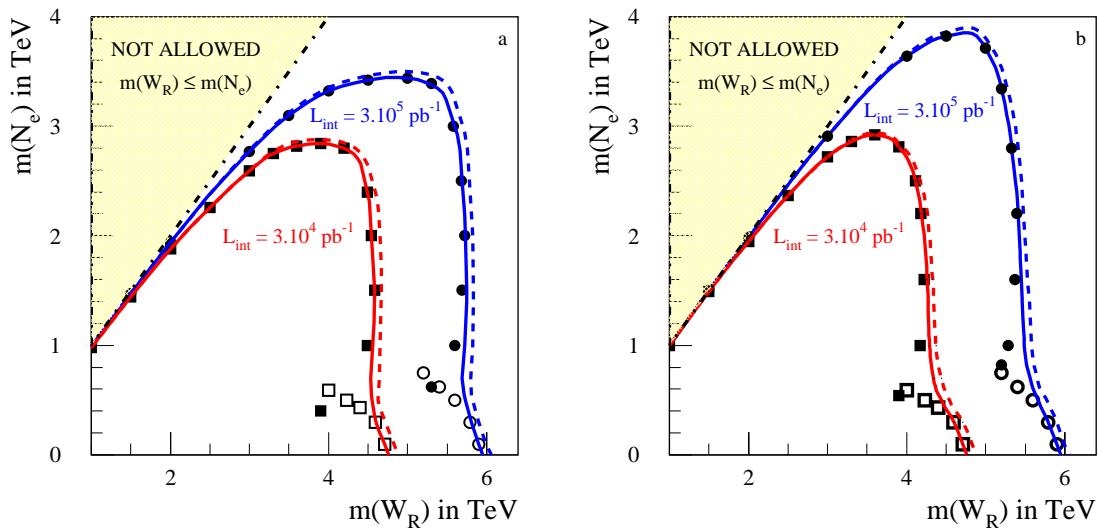


Figure 21-35 Discovery potential for W_R and N_e for 30 fb^{-1} and 300 fb^{-1} . Figures a and b correspond to two different sets of cuts (see text). The full lines correspond to $m(N_e) = m(N_\mu) = m(N_\tau)$ and the dashed lines correspond to $m(N_e) \ll m(N_\mu) \ll m(N_\tau)$ with $m(N_\mu)$ and $m(N_\tau)$ both larger than the W_R mass. The region marked NOT ALLOWED is not accessible using the analysis described here.

Also note that all the background processes lead to two electrons with opposite charges, while $pp \rightarrow W_R \rightarrow e N_e$ leads to two electrons with same-sign charges in half of the cases, due to the Majorana type of N_e . If one also requires that both isolated electrons have the same electric charge, then the background becomes negligible but, on the other hand, half of the signal is lost. After adding this cut, the discovery reach for W_R and N_e is modified, as shown in Figure 21-35b.

In addition to the $pp \rightarrow W_R \rightarrow e N_e$ process, one can also look at the $pp \rightarrow W_R \rightarrow \mu N_\mu$ channel, in order to further improve the sensitivity of ATLAS to the right-handed Majorana neutrinos. For simplicity, only the situation in which $m(N_e) = m(N_\mu) = m(N_\tau)$ is considered and, in order to suppress the background, one requires that the both leptons have the same-sign charge and one applies kinematical cuts at 200 GeV on $m_{inv}(ll)$ and 100 GeV on $E_T(j_1 j_2)$, where l is either an electron or a muon, and on the transverse energy of j_1 and j_2 (see Figure 21-36).

21.6.2.3 Measurement of polarisation effects in $pp \rightarrow W_R \rightarrow e N_e$

If W_R and N_e are discovered, one can then identify the electron coming from W_R in order to measure polarisation effects. In the following, one will assume that the electron coming from N_e is the one for which $m_{inv}(e j_1 j_2)$ is the closest to the reconstructed N_e mass. Once this assignment is done, the fraction of W_R bosons produced in a +1 or -1 helicity state can be determined in the following way. Let y and $\cos\theta$ be the rapidity of the W_R boson and the emission angle of the electron coming from W_R with respect to the beam axis in the centre of mass of the boson. Once they have been measured, one can calculate $F(y)$ and $B(y)$ which are the number of events with $\cos\theta > 0$ and $\cos\theta < 0$ respectively. If A_{FB} is the variable that accounts for the forward-backward asymmetry, then the fraction $X(S_z=+1)$ of W_R bosons produced in the +1 helicity state is simply given by $X(S_z=+1) = 1/2 (1 + 4/3 |A_{FB}|)$. If $m(W_R) = 2$ TeV, then $X(S_z=+1)$ is 77% (71%) for positively charged (negatively charged) W_R bosons, on the generator level. Figure 21-37 shows that, after having suppressed the physics background and having reconstructed the W_R boson, one can account for the polarisation effects, provided that the electron assignment is 100% correct. In real life, it will not be the case, especially when r_W is close to 0.6-0.8: in this case, the invariant masses of $(e_1 j_1 j_2)$ and $(e_2 j_1 j_2)$ are very close, leading to some misidentification for the origin of the two electrons in the final state and thus to some misestimation of $X(S_z=+1)$.

21.6.2.4 Observability of the $pp \rightarrow Z' \rightarrow N_e N_e$ process

If W_R and N_e are discovered and if Z' is also observed, using the $pp \rightarrow Z' \rightarrow l^+ l^-$ process, one can then search for signatures coming from $pp \rightarrow Z' \rightarrow N_e N_e$. In the framework of the Left-Right Symmetric Model, the Z' boson is about 1.7 times heavier than the W_R boson.

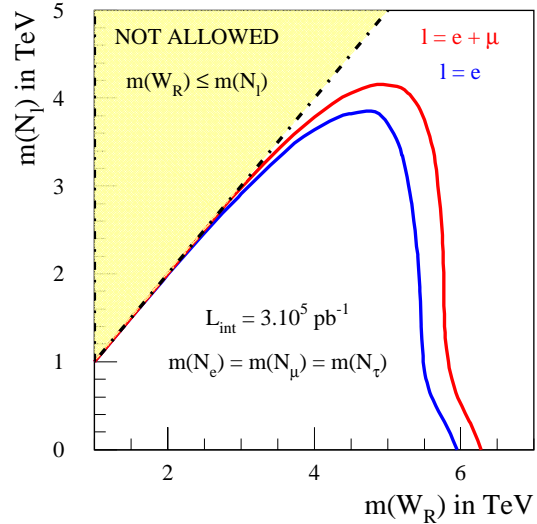


Figure 21-36 The discovery limit for the W_R boson and the right handed Majorana neutrino using the $pp \rightarrow W_R \rightarrow N_\mu$ channel; 300 fb^{-1} assumed and $m(N_e) = m(N_\mu) = m(N_\tau)$. The cuts are the same as in Figure 21-35b.

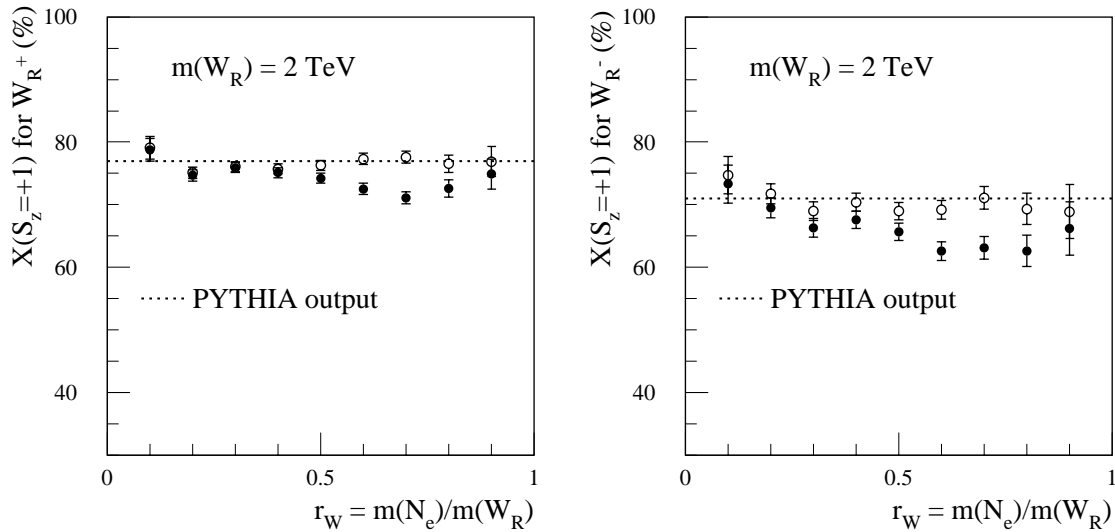


Figure 21-37 Measurement of polarisation effects in the $pp \rightarrow W_R \rightarrow e N_e$ process. The empty circles correspond to a perfect identification of the origin of the electrons and the full circles correspond to a realistic identification of the electrons. The plots are given for an integrated luminosity 300 fb^{-1} with $m(N_e) = m(N_\mu) = m(N_\tau)$. The cuts used to suppress the background are $m_{inv}(ee) > 200 \text{ GeV}$, $E_T(j_1, j_2) > 100 \text{ GeV}$ and $\text{charge}(e_1) = \text{charge}(e_2)$.

If N_e is heavy enough, the final states to look for consist of two electrons and at least four hadronic jets. The assignment of the two electrons and the four hadronic jets to their correct N_e is achieved in the following way: for each of the six possible $(e_1 j_a j_b; e_2 j_c j_d)$ combinations $\delta m(abcd) = |m_{inv}(e_1 j_a j_b) - m_{inv}(e_2 j_c j_d)|$ is calculated and the one that minimises the value of $\delta m(abcd)$ is chosen. The Z' boson is then reconstructed by calculating the invariant mass of the two electrons and the four hadronic jets (see Figure 21-38). Note that, when $m(N_e) \ll m(Z')$, the decay products of the right-handed neutrino are not well separated in the detector and, as a result, a clean signal may be more difficult to extract.

All the processes that lead to final states with two electrons and at least four hadronic jets are potential sources of physics background. In addition to the Standard Model processes described in Section 21.6.2.2, one must take into account $pp \rightarrow W_R \rightarrow e N_e$. When requiring that the invariant masses of the two $(e_1 j_a j_b)$ and $(e_2 j_c j_d)$ selected combinations are very close, this background is suppressed, except if r_W is in the neighbourhood of 0.6-0.8; in this case, the electrons which are produced in the decays of W_R and N_e have similar energies and, once associated with four hadronic jets, they might fake a $N_e N_e$ pair. Thus, one must require either $m_{inv}(ee j_1 j_2) \geq 1.1 m(W_R)$ or $m_{inv}(ee j_1 j_2) \leq (0.9 - 0.2 r_W) m(W_R)$ in order to reduce the main background of the Left-Right Symmetric Model. Note that, by selecting the events with identical electric charges for the two electrons, one does not improve the sensitivity to the $pp \rightarrow Z' \rightarrow N_e N_e$ process.

In addition to the selection criterion on $m_{inv}(e_1 e_2 j_1 j_2)$, a cut at 200 GeV on $m_{inv}(ee)$ and a cut at 100 GeV on E_T of all four jets is applied. Once all the backgrounds are reduced, the $pp \rightarrow Z' \rightarrow N_e N_e$ process may be observed with 30 fb^{-1} of integrated luminosity, if the Z' and N_e masses are smaller than 3.2 TeV and 0.8 TeV respectively. If the integrated luminosity reaches 300 fb^{-1} , then these limits can be pushed up to 4.4 TeV for the Z' mass and 1.2 TeV for the N_e mass (see Figure 21-39).

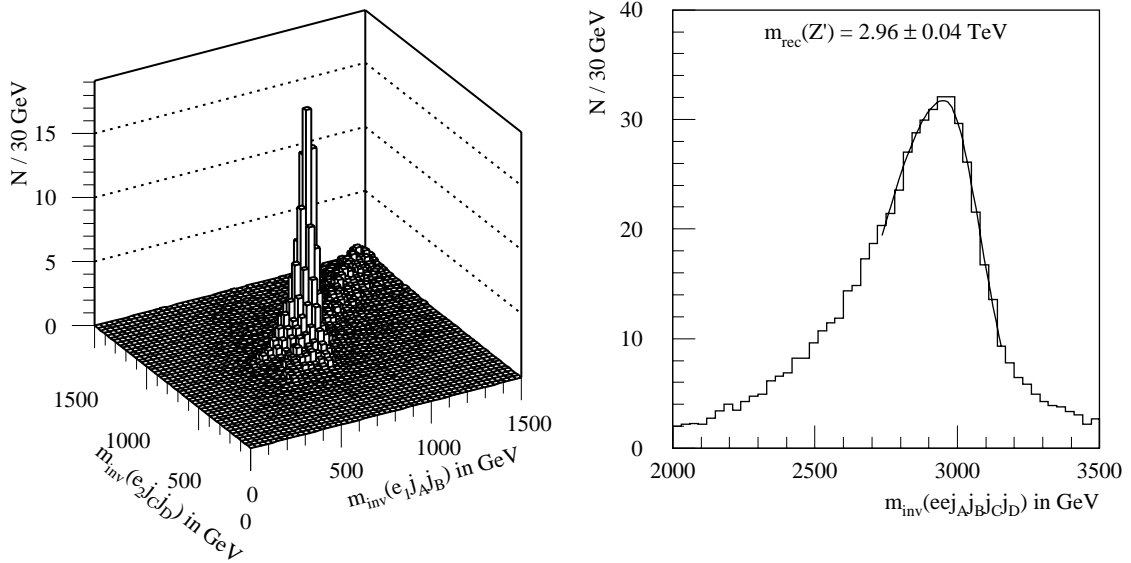


Figure 21-38 Reconstruction of N_e and Z' when their masses are respectively 0.75 and 3 TeV. The plots are given for an integrated luminosity of 300 fb^{-1} and when the three Majorana neutrinos are degenerated in mass. The Z' peak is fitted with an asymmetric Gaussian distribution.

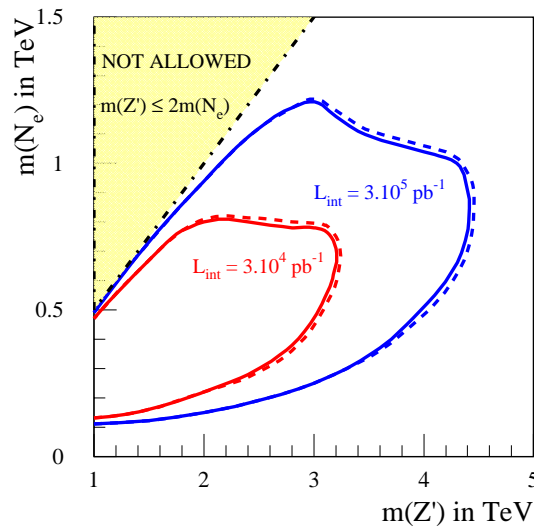


Figure 21-39 Observability of $pp \rightarrow Z' \rightarrow N_e N_e$ for 30 and 300 fb^{-1} of integrated luminosity. The full lines correspond to $m(N_e) = m(N_\mu) = m(N_\tau)$ and the dashed lines correspond to $m(N_e) \ll m(N_\mu) \ll m(N_\tau)$ with $m(N_\mu)$ and $m(N_\tau)$ both larger than the half of the Z' mass.

21.7 Monopoles

The pioneering Dirac paper [21-50] published in 1931 pointed out the possibility of the existence of particles with isolated magnetic charge (monopoles). A monopole restores the symmetry of the Maxwell's equations and explains the quantisation of the electric charge. Secondly, particles with the magnetic charges arise in gauge field theories as soliton like solutions to the field equa-

tions. Such solutions were found by Polyakov [21-51] and t'Hooft [21-52]. This type of monopoles, in realistic Grand Unification Theories have a mass of the order of the unification scale ($\sim 10^{16}$ GeV) and therefore cannot be discovered on the current or future accelerators. So, in the following discussion, Dirac's pointlike monopoles will be considered. Current constraints on monopoles are summarised in Table 21-13.

Table 21-13 Theoretical and experimental limits on monopole masses.

	Theory	Experiment
Charge	$eg = 2\pi n, \quad n = \pm 1, \pm 2, \dots$	
Mass(M/n)	< 7000 TeV (cosmology) > 1.2 TeV [21-55] (deviation from Standard Model)	<u>L3 ($Z \rightarrow \gamma\gamma$)</u> [21-53] < 510 GeV ($J_M = 1/2$) <u>D0</u> [21-54] < 610 GeV ($J_M = 0$) < 810 GeV ($J_M = 1/2$) < 1580 GeV ($J_M = 1$)

In this table, e and g denote electric and magnetic charge, respectively, and units are such that $\alpha_e \equiv e^2/(4\pi) \approx 1/137$ and $\alpha_g \equiv g^2/(4\pi) \approx 34n^2$. Limits on the monopole's mass was obtained in [21-55] for monopole spin $J_M = 1/2$. Experiments searching for monopoles in cosmic rays gives limits on their flux only. Note that the monopole mass always appears in calculations as ratio M/n , so in the following the monopole mass refer to this ratio.

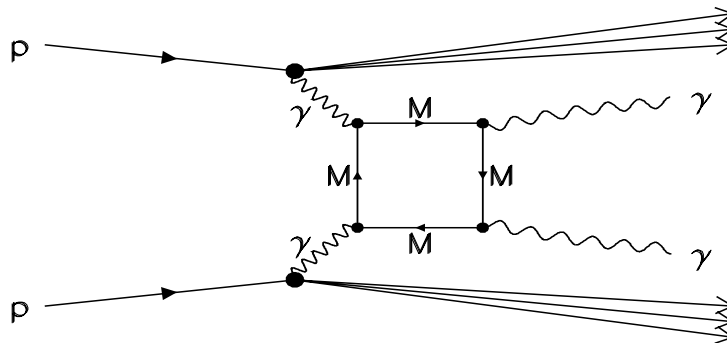


Figure 21-40 Schematic diagram for $\gamma\gamma$ production via the monopole loop.

The current best limit on monopole masses is obtained by the D0 experiment result [21-54], which relies on the method suggested in the paper Ginzburg and Schiller [21-56]. The main idea of this paper is based on observation that the interaction strength between monopole and photon is very strong and could give rise to photon-photon rescattering via the box diagram shown in Figure 21-40. The total cross section

$$\sigma_{pp \rightarrow \gamma\gamma X}(E, M, P, n) = 108P \left(\frac{nE}{M}\right)^8 \left(\frac{N(E)}{N(1\text{TeV})}\right)^2 \left(\frac{1\text{TeV}}{E}\right)^2 \text{fb}$$

shows strong dependence on the energy of incident particles (E) as well as on monopole mass. The numerical factor P reflects dependence of the cross section on monopole spin and equal 0.085, 1.39 and 159 for spin 0, 1/2 and 1, respectively.

The differential spectrum of produced photons as function of transverse momenta is shown on Figure 21-41. The predicted long tail in p_T distribution allows one to work in the region where expected background will be small. Even with p_T cut at 1 TeV about 60% of the signal will survive.

There are a lot of processes which can obscure the signal. First, the same type of processes as shown on Figure 21-40 but with other particles in the loop. This has the same structure as the signal. Fortunately expected cross-section for these process about two orders of magnitude less than the monopole loop for mass region reachable at LHC. (see [21-56] and references therein). There are also processes where direct photons are produced by parton interactions. Finally, there are background processes from detector effects. These are:

- production of a photon and a hadron jet, mis-identified as electromagnetic one;
- production of two hadron jets both mis-identified as electromagnetic ones.

The probability to misidentify hadron jet as an electromagnetic one was taken to be 0.1% which is conservative but adequate for this analysis.

Monte Carlo estimation for background processes was made by ATLFast with PYTHIA as event generator. Events were selected according to the following criteria:

- there are two isolated photons with $E_T > 50$ GeV;
- no additional jet or muon with $E_T > 25$ GeV;
- missing transverse energy less than 50 GeV.

To illustrate how monopole induced events will modify the distribution, Figure 21-42 shows the expected event rate for 100 fb^{-1} of integrated luminosity, assuming monopole mass equal to 10 TeV. They are shown as a function of S_T the scalar sum of photon transverse momenta. For a particular choice $S_T > 2$ TeV The signal sensitivity, defined as $S/(\sqrt{B})$ as function of the monopole mass presented on Figure 21-43. It is clear that at LHC limits significantly in excess of the current ones will be set.

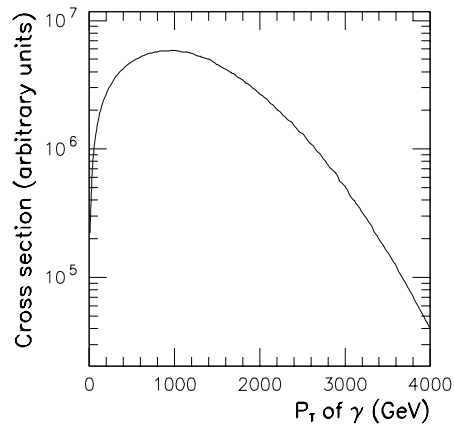


Figure 21-41 Theoretical prediction for transverse momenta spectra of photons.

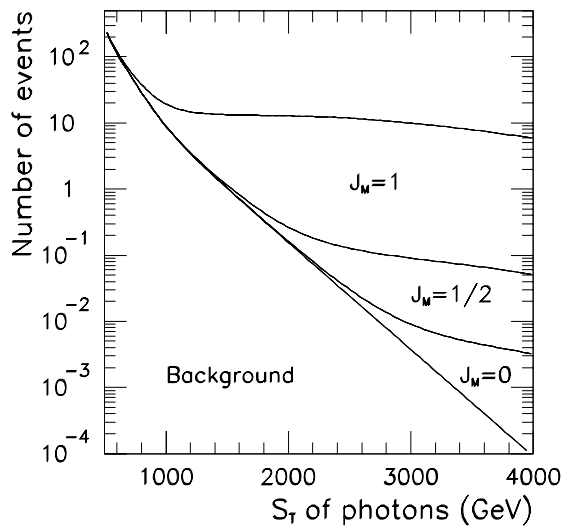


Figure 21-42 Expected number of events from background and background plus signal for 100 fb⁻¹. Mass of monopole as taken as $M/n = 10\text{TeV}$.

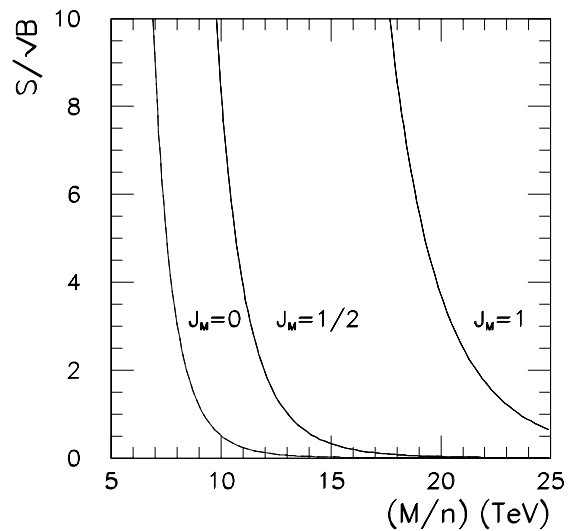


Figure 21-43 Signal sensitivity as function of monopole mass.

21.8 References

- 21-1 S. Weinberg, Phys Rev. **D19**, (1979) 1277;
L. Susskind, Phys. Rev. **D20** (1979) 2619.
- 21-2 S. Dimopoulos and L. Susskind, Nucl. Phys. **B155** (1979), 237;
E. Eichten and K. Lane, Phys. Lett. **B90** (1980) 125.
- 21-3 E. Eichten, K. Lane and J. Womersley, Phys.Lett. **B405** (1997) 305.
- 21-4 B.A. Dobrescu and J. Terning, Phys.Lett. **B416** (1998) 29.
- 21-5 M. Golden and L. Randall, Nucl. Phys. **B361** (1991) 3;
R.S. Chivukula *et al.*, hep-ph/9305232 or Phys.Lett. **B311** (1993) 157.
- 21-6 K. Lane, 27th International Conference on High Energy Physics (ICHEP), Glasgow, Scotland, 1994 (hep-ph/9409304).
- 21-7 M. Knecht and E. de Rafael, Phys.Lett. **B424** (1998) 335.
- 21-8 C. T. Hill, Phys. Lett. **266B** (1991) 419.
- 21-9 K. Lane and E. Eichten, Phys. Lett. **B352** (1995) 382.
- 21-10 R. Casalbuoni *et al.*, hep-ph/9809523;
T.L. Barklow *et al.*, hep-ph/9704217 (Working group summary report from the 1996 DPF/DPB Summer Study, 'New Directions in High Energy Physics' Snowmass, Colorado);
K. Cheung and R.M. Harris, Summary of New Interactions subgroup of New Phenomena group at Snowmass. To appear in the proceedings of DPF/DPB Summer Study on New Directions for High Energy Physics, Snowmass, Colorado, 1996;
R. Chivukula *et al.*, (in 'Electroweak Symmetry Breaking and New Physics at the TeV Scale', World Scientific, T. Barklow, ed., 1996).

- 21-11 T. Sjostrand, *Comp. Phys. Commun.* **82** (1994) 74. The most recent version is obtained from <http://www.thep.lu.se/tf2/staff/torbjorn/Pythia.html>
- 21-12 E. Richter-Was *et al.*, 'ATLFAST, a package for particle-level analysis'. ATLAS Internal Note PHYS-No-079(1996).
- 21-13 K. Lane, 'Electroweak and flavour dynamics at hadron colliders', hep-ph/9605257, 'Non-supersymmetric extensions of the Standard Mode', hep-ph/9610463
- 21-14 E. Eichten and K. Lane, *Phys. Lett.* **B388** (1996) 803.
- 21-15 K. Lane, 'Technihadron production and decay in low scale technicolour', hep-ph/9903369.
- 21-16 S. Mrenna and J. Womersley, *Phys.Lett.* **B451** (1999) 155.
- 21-17 R.M Harris.' Discovery mass reach for topgluons decaying into B-anti-B at the Tevatron'. hep-ph/9609316.
- 21-18 E. Eichten, I. Hinchliffe, K. Lane and C. Quigg, *Rev. Mod. Phys.* **56** (1984) 579; *Rev. Mod. Phys.* **58** (1985) 1065.
- 21-19 T. Appelquist and G. Triantaphyllou, *Phys. Rev. Lett.* **69** (1992) 2750.
- 21-20 F. Abe *et al.*, 'Search for a technicolor omega(T) particle in events with a photon and a b-quark jet at CDF', hep-ex/9810031.
- 21-21 Thanks to M. Mangano for providing the Monte Carlo program for generation of $\gamma b\bar{b}$ background.
- 21-22 S. Slabospitsky, ATLAS note in preparation.
- 21-23 U. Baur, I. Hinchliffe and D. Zeppenfeld, *Int. J. Mod. Phys.* **A2**, (1987) 1285; U. Baur, M. Spira and P. Zerwas, *Phys. Rev* **D42**, (1990) 815.
- 21-24 O. Cakir and R. Mehdiyev, 'A search for excited quarks at the CERN LHC', ATLAS Internal Note ATL-PHYS-99-002.
- 21-25 CDF Collaboration, F. Abe *et al.*, *Phys. Rev. Lett.* **72** (1994) 3004.
- 21-26 D0 Collaboration, I. Bertram, Report No. Fermilab-Conf-96/389-E, (1996).
- 21-27 CDF Collaboration, F. Abe *et al.*, *Phys. Rev.* **D55** (1997) R5263; CDF Collaboration, F. Abe *et al.*, *Phys. Rev. Lett.* **74** (1995) 3538.
- 21-28 L.F.Abbott and E.Farhi *Phys. Lett.* **B101** (1981) 69; *Phys. Lett.* **B189** (1981) 547; J. Pati and A. Salam, *Phys. Rev.* **D10** (1974) 275; E. Witten, *Nucl.Phys.* **B258** (1985) 75; M. Dine *et al.*, *Phys.Lett.* **B259** (1985) 519; J. Breit, B.A.Ovrut and G. Segre, *Phys.Lett.* **B158** (1985)33; S.Pakvasa, *Int. J. Mod. Phys.* **A2** (1987) 1317.
- 21-29 J.L. Hewett and S. Pakvasa *Phys. Rev.* **D37** (1988) 3165.
- 21-30 E. Tsemmelis, 'Further Studies in Detecting Singly-produced Scalar leptoquarks with the ATLAS Detector', ATLAS Internal Note PHYS-NO-029 (1993).
- 21-31 A. d'Avella, 'Study of Scalar leptoquark pair production at LHC', ATLAS Internal Note PHYS-NO-026 (1993).
- 21-32 CDF Collaboration, F. Abe *et al.*,*Phys.Rev.Lett.* **77** (1996) 5336.
- 21-33 D0 Collaboration, B. Abbott *et al.*,*Phys.Rev.Lett.* **80** (1998) 666.
- 21-34 UA1 Collaboration, C. Albajar *et al.*, *Phys. Lett.* **B209** (1988) 127.

- 21-35 UA2 Collaboration, J. Alitti *et al.*, *Z. Phys.* **C49** (1991) 17.
- 21-36 CDF Collaboration, F. Abe *et al.*, *Phys. Rev* **D41** (1990) 1722, *Phys. Rev. Lett.* **71** (1993) 2542.
- 21-37 Z.U. Usubov, 'A search for quark compositeness at the LHC', ATLAS Internal Note ATL-COM-PHYS-99-052 (1999).
- 21-38 E. Eichten, K. Lane and M. Peskin, *Phys. Rev. Lett.* **50** (1983) 811;
E. Eichten *et al.*, *Rev. Mod. Phys.* **56** (1984) 579.
- 21-39 M. Bosman, VI Int.Conf. on Calorimetry in HEP - Frascati, June 8-14, 1996, Frascati Physics series Vol.VI,(pp.299-310)
- 21-40 F. Ariztizabal *et al.*, *Nucl. Instr. and Meth.* **A349** (1994), 384.
- 21-41 E.C. Katsoufis, 'Searching for Quark-Lepton Compositeness at LHC', ATLAS Internal Note ATLAS-PHYS-NO-038 (1994).
- 21-42 J.C. Pati, and A.Salam, *Phys. Rev.* **D10** (1974) 275;
R.N. Mohapatra, and J.C. Pati, *Phys. Rev.*,**D11** (1975) 566 and *Phys. Rev.* **D11** (1975) 2558;
G. Senjanovic, and R.N. Mohapatra:, *Phys. Rev.* **D12** (1975) 1502;
G. Senjanovic: *Nucl. Phys.* **B153** (1979) 334.
- 21-43 G. Altarelli, B. Mele, and M. Ruiz-Altaba: *Z. Phys.* **C45** (1989) 109.
- 21-44 A. Henriques and L. Poggioli, 'Detection of the Z' vector boson in the jet decay mode ($Z' \rightarrow q\bar{q}$) ($q \rightarrow jj$). Resolution and pile-up studies' ATLAS Internal Note PHYS-92-010 (1992).
- 21-45 M.C. Cousinou, 'Search for W' in the lv channel', ATLAS Internal Note PHYS-94-059 (1994)
- 21-46 R.N. Mohapatra and G. Senjanovic, *Phys. Rev.* **D23** (1981) 165.
- 21-47 R.N. Mohapatra and P.B. Pal, 'Massive neutrinos in physics and astrophysics (World Scientific, Singapore, 1991);
C.W. Kim, A. Pevsner, 'Neutrinos in physics and astrophysics' (Harwood Academic Publishers, Switzerland, 1993).
- 21-48 R. Kuchimanchi and R.N. Mohapatra, *Phys. Rev.* **D48** (1993) 4352 and *Phys. Rev. Lett.* **75** (1995) 3989.
- 21-49 A. Datta and M. Guchait, D.P. Roy, *Phys. Rev.* **D47** (1993) 961;
J. Collot, and A. Ferrari, ATLAS Internal Note PHYS-98-124
- 21-50 P.A.M. Dirac, *Proc. R. Soc., London*, **A133** (1931) 60.
- 21-51 A.M. Polyakov, *JETP Lett.*, **20** (1974) 194.
- 21-52 G. t'Hooft, *Nucl. Phys.*, **B79** (1974) 276.
- 21-53 M. Acciarri *et al.*, *Phys. Lett.*, **B345** (1995) 609.
- 21-54 B. Abbott *et al.*, *Phys. Rev. Lett.* **81** (1998) 524.
- 21-55 A. De Rujula, *Nucl. Phys.* **B435** (1995) 257.
- 21-56 L.F. Ginzburg and A. Schiller, *Phys. Rev.*, **D57** (1998) 6599.